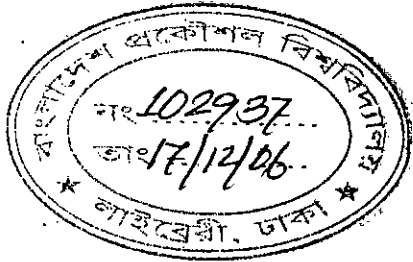


Performance Analysis of InGaAsP/InP Quantum Wire Electro Absorption Modulators

A thesis submitted to
the Department of Electrical and Electronic Engineering
of
Bangladesh University of Engineering and Technology
in partial fulfillment of the requirement
for the degree of
MASTER OF SCIENCE IN ELECTRICAL AND ELECTRONIC ENGINEERING



by

Arif Mohammad Sonnet


DEPARTMENT OF ELECTRICAL AND ELECTRONIC ENGINEERING
BANGLADESH UNIVERSITY OF ENGINEERING AND TECHNOLOGY

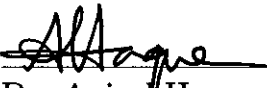
2006

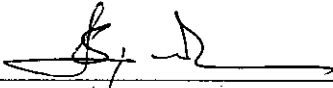



The thesis titled “ Performance Analysis of InGaAsP/InP Quantum Wire Electro Absorption Modulators” Submitted by Arif Mohammad Sonnet, Roll No.: 040306253P, Session: April 2003 has been accepted as satisfactory in partial fulfillment of the requirement for the degree of MASTER OF SCIENCE IN ELECTRICAL AND ELECTRONIC ENGINEERING on August 06, 2006.

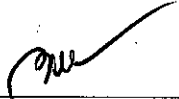
BOARD OF EXAMINERS

1. 

Dr. Quamrul Huda
Professor
Department of Electrical and Electronic Engineering
BUET, Dhaka-1000, Bangladesh. **Chairman**
(Supervisor)
2. 

Dr. Anisul Haque
Professor and Chairperson
Department of Electrical and Electronic Engineering
East West University, Dhaka-1212, Bangladesh. **Member**
(Co-Supervisor)
3. 

Dr. Satya Prasad Majumder
Professor and Head
Department of Electrical and Electronic Engineering
BUET, Dhaka-1000, Bangladesh. **Member**
(Ex-officio)
4. 

Dr. Md. Shafiqul Islam
Professor
Department of Electrical and Electronic Engineering
BUET, Dhaka-1000, Bangladesh. **Member**
5. 

Dr. Md. Abu Hashan Bhuiyan
Professor
Department of Physics
BUET, Dhaka-1000, Bangladesh. **Member**
(External)

Declaration

I hereby declare that this thesis or any part of it has not been submitted elsewhere for the award of any degree or diploma.

Signature of the candidate


06/08/2006

(Arif Mohammad Sonnet)

Dedication

To My Parents.

Acknowledgement

I wish to convey my heartiest gratitude and profound respect to my co-supervisor Dr. Anisul Haque and my supervisor Dr. Quamrul Huda for their continuous guidance, suggestions and wholehearted supervision throughout the progress of this work, without which this thesis never be possible. Originally this research was supervised by Dr. Haque. The research was already in advanced stage when Dr. Haque left BUET joining East West University as chairman of the Dept. of EEE. I am grateful to him for acquainting me with the world of advanced research.

I am grateful to Mr. Abul Hussain, Associate Professor and Head, Dept. of EEE, Ahsanullah University of Science and Technology (AUST), who provided with all the facilities of VLSI laboratory of the department and cooperation to complete the work. In this regard, I also like to express thanks and gratitude to Dr. Satya Prasad Majumder, Professor and Head, Dept. of EEE, BUET.

I want to thank my friends Md. Lutful Hai, M. Abul Khayer, and all my friends and colleagues of AUST, who were directly or indirectly related to this work, for their support and encouragement. Last but not the least, I would like to express my gratitude to my parents for their encouragement and love throughout my entire life.

Contents

Declaration	ii
Dedication	iii
Acknowledgement	iv
Abstract	x
1 Introduction	1
1.1 Literature Review	4
1.2 Objective of the Work	8
1.3 Organization of the Thesis	9
2 Theory	10
2.1 Schrödinger Equation and the Multiband Hamiltonian	10
2.1.1 The Hamiltonian Matrix	12
2.1.2 The Hamiltonian Matrix Elements	13
2.2 Strain Analysis	14
2.2.1 Strain Effect on Electronic States	14
2.3 The Electron-Photon Interaction	16
2.4 The Gain/Absorption Spectrum	16
3 Calculation Procedure	19
3.1 Material Properties of GaInAsP/InP Systems	19

3.1.1	Interpolation of Material Constant	19
3.2	Analytical Expressions for Strain Distribution	21
3.3	Electronic States of Semiconductor Hetero-structures	25
3.4	Transition Matrix Elements	28
3.5	The Gain/Absorption Spectra	29
3.6	Bandgap Reduction Due to Application of Electric Field	30
3.7	Calculation of Extinction Ratio	31
4	Results and Discussion	33
4.1	Electronic States of QWires EAMs	33
4.2	Effect of Electric Field on Band Structure of QWire EAMs	35
4.3	Absorption Characteristics	43
5	Conclusions	51
5.1	Summary	51
5.2	Suggestions for Further Work	53
	Bibliography	54

List of Figures

3.1	Schematic structure of a QWire EAM integrated with QWire laser and Distributed Bragg Reflector sections.	20
3.2	Cross-sectional schematic diagram of a vertical stack of multiple QWire structures.	21
3.3	Cross-sectional schematic diagram of a strained QWire structure.	23
4.1	Dispersion relationships for the lowest two conduction and highest three valence band energy levels for 20 nm wide QWire EAMs (a)-(b) and 30 nm wide QWire (c)-(d) calculated for two different types of barriers.	34
4.2	Dispersion relationships for the lowest conduction and the highest three valence band energy levels for 20 nm wide QWire (a-b) and 30 nm wide QWire (c-d) calculated for both zero and 125 KV/cm electric field. Two different types of barriers are considered.	37
4.3	Electric field dependence of effective bandgap in 10 nm, 30 nm and 50 nm wide QWire EAMs for LM (a-c) and 0.15% TS (d-f) barriers. Single stack structures are considered.	38

4.4	Electric field dependence of effective bandgap in 10 nm, 15 nm, 20 nm, 30 nm, 40 nm and 50 nm wide QWire EAMs for LM barrier calculated using the numerical method and Eqs. (4.1)-(4.3).	40
4.5	Electric field dependence of the effective bandgap in 10 nm, 30 nm, 50 nm for 0.15% TS barrier (a)-(c) and for 0.30% TS barrier (d)-(f) calculated using the numerical method and Eqs. (4.1)-(4.3).	41
4.6	Electric field dependence of the effective bandgap in 10 nm, 30 nm, 50 nm for LM barrier with $L_z=9$ nm (a)-(c) and for 0.15% TS barrier with $L_z=8$ nm (d)-(f) calculated using the numerical method and Eqs. (4.1)-(4.3).	42
4.7	Transition matrix elements M_{II} as functions of wave vector k in a 20 nm wide QWire for three types of barriers (a) and for different number of QWire layers with 0.15% TS barriers (b). Only $TE_{ }$ polarization is considered.	44
4.8	Absorption as a function of photon wavelength showing the effects of applied electric field in single layer QWire EAMs with 0.15% TS Barrier for different wire widths.	45
4.9	Absorption as a function of photon wavelength showing the effects of applied electric field in 20 nm wide QWire EAMs (a), (b) and 30 nm wide QWire EAMs (c), (d) for two different types of barriers. Single layer structure and both LM and 0.15% TS barriers are considered.	46

4.10 Absorption as a function of photon wavelength showing the effects of applied electric field in 20 nm wide QWire EAMs (a)-(c) and 30 nm wide QWire EAMs (d)-(f) with 0.15% TS barrier for different number of layers in the active regions. . . .	47
4.11 Absorption per layer as a function of photon wavelength showing the effects of applied electric field in a QWire EAMs with different wire height with 0.15% TS Barrier.	48

3

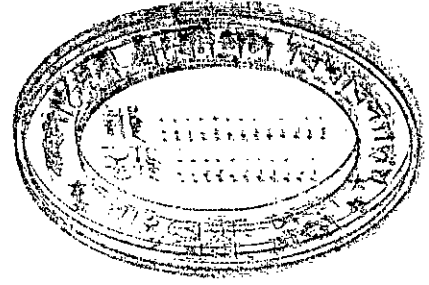
List of Tables

3.1	Material Constant	22
4.1	Comparison of key dispersion relationship parameters for 10 nm, 20 nm, and 30 nm QWires	35
4.2	Coefficients of the Eq. (4.2) for the variable a and b of Eq. (4.1)	39
4.3	Extinction ratio of QWire and QWell EAMs with $L_z=7\text{nm}$ for $F_S=125\text{ KV/cm}$. Length of the EAM section is $500\ \mu\text{m}$	49

Pc

Abstract

Performance of compressively strained (CS) GaInAsP/InP quantum wire (QWire) electro absorption modulators (EAMs) is theoretically investigated. The electric field dependence of the effective bandgap of QWire EAMs (quantum confined Stark effect) is studied using an 8 band $\mathbf{k}\cdot\mathbf{p}$ theory including elastic strain relaxation effects. Elastic strain relaxation is calculated using an analytical approach. An empirical relationship is proposed for the effective bandgap for quick and accurate estimation of the Stark shift. The relationship is verified through numerical simulations. Different quantities such as, the absorption coefficient, the extinction ratio and the operating wavelength are calculated as function of device parameters for performance analysis of the QWire EAMs. Polarization insensitivity is not required to be achieved in the EAMs and the EAMs are designed for absorption of transverse electric (TE) radiation, which is the polarization of light output from QWire lasers fabricated on the same substrate in a photonic integrated circuit. It is observed that significant increase in the extinction ratio can be achieved by adopting QWires in EAMs. In spite of higher absorption peaks, narrower wires exhibit lower extinction ratios due to the reduced value of the in-plane occupation factor. This situation may be improved by increasing the packing density of the QWires. Our results are useful for optimizing device design through proper choice of device parameters to meet a certain requirement.



Chapter 1

Introduction

The requirements for optical communication systems are increasing at an extraordinary rate due to continuously increasing demand for long-haul transmission and high bit rates. Since the optical fiber potential for multiterabit communication was recognized in the 70s, much has been done to optimize the different components involved in the optical communication systems in order to reach the goal. One fundamental function to be performed by the optical system is the modulation of the light so that information is transmitted. Electro absorption modulators (EAMs) have been shown to be useful in fiber-optic link operation near either $1.3 \mu\text{m}$ or $1.55 \mu\text{m}$ for both analog and digital signal transmission. They are small in size and can be integrated with the laser diode, while being effective in changing the light intensity as a function of applied electric field.

The phenomena of transferring energy of a photon to an electron, elevating it from some state in the valence band to some state in the conduction band is known as stimulus absorption. [1]. Such stimulus absorption events generate new carriers and are also responsible for the disappearance of pho-

tons, creating an upward transition of electron from the valence band to the conduction band.

Franz-Keldysh effect (FKE) describes the electron-hole excitation with below bandgap photons due to lateral tunnelling with an applied electric field [1]. The extension of carrier wave function in the forbidden energy gap in the presence of an applied field is realized by FKE. FKE describes that applied electric field in bulk semiconductor broadened the band edge absorption. Thus the application of reverse bias field lowers the absorption edge and reduces the emitting light. This change in the optical absorption can be employed in optoelectronic modulators.

When semiconductors are fabricated in very thin layers (e.g., 100 Å), the optical absorption spectrum changes radically as a result of quantum confinement of carriers in the resulting one-dimensional potential wells. In such multi quantum wells (MQWs), the confinement changes the density of states (DOS) from the smooth function of bulk material to a series of steps. Additionally, the confinement also increases the effective bandgap energy. When electric field is applied perpendicularly to the layers of quantum wells (QWell), it significantly changes effective bandgap energies between electrons and holes confined in the well region. This effect is referred to as the quantum confinement Stark effect (QCSE) [1]. Change in the effective bandgap also changes the absorption spectrum. MQW EAMs are very attractive for applications requiring high-speed modulation of laser light with high efficiency [2] - [4]. Improved performances such as low drive voltage, high field sensitivity, stronger absorption, high extinction ratio are achieved using MQW EAMs [5].

Recent progress in epitaxial growth and process techniques is making it possible to realize quaternary quantum wire (QWire) structures where carriers are confined two-dimensionally. Strain-compensated (SC) MQWire lasers have successfully been realized practically with a fabrication method which combines electron beam lithography (EBL), CH_4/H_2 reactive ion etching (RIE) and organometallic vapor-phase-epitaxial (OMVPE) regrowth [6]. This method is very attractive for GaInAsP/InP based devices consisting of low dimensional active regions.

QWire structures attract much interest due to their novel physical properties and consequent improvements of device performance. By using QWires in semiconductor lasers, higher gain and lower threshold current is expected [7]. Consideration of strain effects on band structures is important in these kinds of structures when the wires are buried in larger band gap materials with different lattice constants. These are referred to as strained wires. In strained wires, strain can also exist in the surrounding matrices as well as in the wires. Also improvements that can be achieved by adopting strained QWells in lasers [8]- [9], may also be expected in strained QWires [10]. Accordingly, it is important to study the strain effect in QWires. Strain relaxation in EAM structures, whereby material reverts wholly or partially to its preferred lattice spacing, may lead to modifications of the electronic band structures.

As in QWire structures, the carriers are confined in two dimensions, the Density of States (DOS) is modified and exhibits different characteristics than the DOS in bulk or QWell structures. It is expected that because of the higher degree of confinement in QWires, QWire EAMs may also perform

better than QWell EAMs. While much attention has been paid to QWell EAMs, comparatively less work has been done on QWire EAMs, perhaps due to the difficulties in fabricating QWire EAMs. However, the fabricating technology for strained QWire, as described in [6], is particularly suitable for constructing photonic integrated circuits involving low dimensional active regions [11, 12]. In such systems, the semiconductor laser, the high-reflectivity Bragg reflector and QWire EAM may be monolithically integrated exploiting the blue shift of the effective bandgap with reducing wire width.

1.1 Literature Review

Semiconductor EAMs are one of the most successful photonic devices benefited by the quantum-size effect, since their operation characteristics have been drastically improved by the introduction of QWell structures. Miller *et al.* [2] presented the theory and extended experimental results for the large shift of optical absorption in quantum well structures with electric field perpendicular to the active layers. They have shown the experimental results of the shift of the absorption peaks for a field strength up to ~ 10 KV/cm. Comparing theory and experiment they found excellent agreement for the shift of absorption spectrum with applied field in MQW.

Chiu *et al.* [5] proposed a travelling-wave electrode structure EAM to achieve high bandwidth with lower drive voltages at $1.55 \mu\text{m}$ wavelength. They fabricated an InGaAsP/InGaAsP MQW travelling-wave electro absorption modulator with a bandwidth above 20 GHz. They demonstrated a drive voltage of 1.2 V for an extinction ratio of 20 dB.

Mendez *et al.* [13] performed the low temperature photoluminescence

(PL) measurements in narrow GaAs–Ga_{1-x}Al_xAs QWells subjected to an electric field perpendicular to the well plane. They found that with the increasing electric field the PL intensity decreases and becomes completely quenched at a field of few tens of KV/cm. They also performed variational calculation in order to qualitatively explain the experimental observations.

Wiedenhaus *et al.* [14] presented different strategies for simulation of electro absorption modulators, which allow an efficient and adequate analysis of the most important physical aspects of such devices. They demonstrated that the direct solution of the density matrix, coupled to the semiconductor equations, is suitable for investigating nonlinear effects. The time-dependent problem is solved by implicit, rather than by explicit algorithms as the latter demand very restrictive stability conditions.

Pappert *et al.* [15] demonstrated a ridge-waveguide In_{0.53}Ga_{0.47}As/InP MQW EAMs operating at a wavelength of 1.52 μm . Previous experimental works on 1.5 μm MQW waveguide primarily examined the modulation performance of TE polarized light while not as much attention has been paid to TM polarization. The polarization dependence of the electro absorption for an InGaAs/InAlAs MQW waveguide modulator has been reported [16] with similar modulation performance achieved for both polarization. The EAM presented here exhibits 24.5 dB extinction ratio at 10 V bias voltage for TM polarization which is 20 times that of TE mode at the same applied bias voltage.

Ido *et al.* [17] demonstrated the improved modulation properties of a new strained InGaAs/InAlAs MQW EAMs. They proposed a novel approach to lower the driving voltage with the introduction of tensile strain into the

ternary InGaAs wells. They have shown that the bandgap wavelength shift under applied voltage in the strained MQW modulator is much larger than in the unstrained MQW modulator. This strain enabled them to achieve polarization independent modulation.

Wakita *et al.* [18] has demonstrated the improved properties of strain-compensated InGaAs–InAlAs MQW EAMs. MQW layers used here consists of ten 12 nm thick undoped 0.5% tensile strained $\text{In}_{0.53}\text{Ga}_{0.47}\text{As}$ and eleven 5 nm thick 0.5% compressively strained $\text{In}_{0.60}\text{Al}_{0.40}\text{As}$ barriers. The EAM presented here exhibits low polarization dependence with an extinction ratio difference between TE and TM polarization of less than 1 dB and the modulator can operate at a large modulation frequency, greater than 20 GHz.

Ravikumar *et al.* [19] reported the field induced absorption coefficient variation spectra in an unstrained, a 0.15%, a 0.30% a 0.45% tensile-strained InGaAs/InP throughout the spectral range near and away from the bandgap. They found that the wavelength difference between the absorption coefficient variation peak for the TE and TM mode varies linearly with the strain, showing nearly zero value for 0.3% tensile strain. Thus they demonstrated that the wavelength difference can be engineered by a proper choice of tensile strain and it is possible to control the polarization characteristics of the field induced absorption coefficient variation and hence the index variation in a QWell structure.

Chang *et al.* [20] theoretically investigated the quantum-confined Stark effect in GaAs/ $\text{Al}_x\text{Ga}_{1-x}\text{As}$ quantum wires formed in V-grooved structures. They applied a numerical method to calculate the exciton states of the V-

shaped quantum wires within the effective mass envelope function theory in the presence of electric field. They proposed two factors, the asymmetric geometry of wire cross section and the electric field induced coulomb interaction, for the possible mechanism of the shifts of PL peaks of the wire modulator.

Weman *et al.* [21] studied the electric field effect in GaAs V-groove quantum wires by PL and linearly polarized PLE. In PLE spectra they observed a large redshift as well as field dependent polarization anisotropy. They used a 2D quantum confined Stark effect model in order to explain the energy shifts of the ground state as well as higher excited states.

Huang *et al.* [22] presented the simulation of InGaAs-InP quantum wire Stark effect optical modulators showing a novel trend. They computed the absorption coefficient and the change of the refractive index in $\text{In}_{0.33}\text{Ga}_{0.67}\text{As}$ -InP quantum wires involving exciton transitions resulting in Stark effect electro-optic modulators. They have found that the exciton binding energy and electric field induced refractive index change is significantly higher compared to InGaAs based quantum well system.

Arakawa *et al.* [23] investigated the quantum confined Stark effect in GaAs quantum wires formed in a V-groove structure, demonstrating observations of a blue shift of the photoluminescence peak with the increase of electric fields at 50 K. This blue shift is attributed to the fact that the change in enhanced binding energy of excitons due to the electric field is larger than that in quantized energy levels of electrons and holes. They also measured the time-resolved photoluminescence. They demonstrated that the photoluminescence decay time is decreased in small quantum wires of 8 nm

width with the increase of electric fields, while the decay time is increased in the quantum wires with a size of 35 nm. These results indicate that the escaping of carriers is more dominant in smaller structures than reduction of the oscillator strength due to the electric fields.

Vázquez *et al.* [24] presented a theoretical calculation of the shift of energy levels of electrons in cylindrical quantum wires with an electric field applied transversely to the axis of cylindrical symmetry. They performed a variational calculation to obtain the shift in the ground-state energy of the carriers due to the electric field using infinite confining potential. They found a nonlinear shift of energy levels with the electric field for low electric field, while for strong field the Stark shift of the ground state energy increases almost linearly with the electric field.

1.2 Objective of the Work

The objective of this work is to theoretically analyze the performance of GaInAsP/InP compressively strained (CS) QWire EAMs. The study is motivated by the potential of incorporating these devices in photonic integrated circuits containing QWire lasers [11], [12]. In order to evaluate the performance of the QWire EAMs, different parameters such as, absorption coefficient, extinction ratio, operating wavelength etc. are calculated using an 8 band $\mathbf{k}\cdot\mathbf{p}$ theory. An empirical relationship is proposed to quickly estimate the field induced shift in the effective bandgap. The performance parameters of strained QWell EAMs are also calculated and compared to those of QWire EAMs to identify the improvement caused by the additional carrier-confinement in QWires. Effects of non-parabolicity due to material

properties, quantum-confinement and elastic strain relaxation are incorporated in the calculation. Finally, we investigate the effects of variation of device parameters, such as, QWire width, strain, multi-well stack, etc. on the extinction ratio which allows optimizing device design.

1.3 Organization of the Thesis

This thesis consists of five chapters. Chapter 1 gives an introduction followed by literature review and the objective of the work. The basic theory behind this work is discussed in Chapter 2. Theories to model the strained QWire and QWell quaternary EAMs are presented in this chapter. Chapter 3 deals with the device structure along with a detailed discussion on the procedures followed to develop the proposed model and the calculation procedure of the work. Results and discussion are presented in Chapter 4. Conclusive remarks and discussions are presented in chapter 5. A recommendation for future study is also suggested here.

Chapter 2

Theory

In this chapter the theory concerning the calculation of the optical gain and absorption of QWell and QWire electro absorption Modulators (EAMs) is described.

2.1 Schrödinger Equation and the Multiband Hamiltonian

The electron wavefunctions in the conduction and valence bands are found in principle by solving the Schrödinger equation:

$$H_0 = \left[\frac{\mathbf{p}^2}{2m_0} + V(\mathbf{r}) \right] \Psi = E\Psi. \quad (2.1)$$

where \mathbf{p} is the momentum operator, \mathbf{r} is the position vector, m_0 is the free electron mass and, Ψ is the wavefunction of the electron and $V(\mathbf{r})$ is the potential energy of the electron.

The electronic states and the energy levels of the QWell, QWire and QDot semiconductor devices are explicitly found by solving the multiband effective

mass equation [25].

$$E\psi_\nu(\mathbf{r}) = \sum_{\nu'} H_{\nu\nu'}(-i\nabla)\psi_{\nu'}(\mathbf{r}) + U(\mathbf{r})\psi_\nu(\mathbf{r}). \quad (2.2)$$

where ν represents the band index and $H_{\nu\nu'}(\mathbf{k})$ is defined as

$$H_{\nu\nu'}(\mathbf{k}) = \begin{cases} \frac{\hbar^2 k^2}{2m_0} + E_{\nu 0}, & \nu = \nu' \\ \hbar \frac{P_{\nu\nu'} \cdot \mathbf{k}}{m_0}, & \nu \neq \nu' \end{cases} \quad (2.3)$$

$P_{\nu\nu'}$ is known as the momentum matrix elements between bands ν' and ν and is defined as

$$P_{\nu\nu'} = -i\hbar \langle \bar{u}_{\nu,0} | \nabla \bar{u}_{\nu',0} \rangle. \quad (2.4)$$

Where $u_{\nu,0}$ is known as the zone center Bloch function of the band ν . the relation between the actual wavefunction and the multiband envelope functions follows readily from

$$\Psi_0(\mathbf{r}) = \sum_{\nu} u_{\nu,0}(\mathbf{r})\psi_\nu(\mathbf{r}) \quad (2.5)$$

Eq. (2.2) can be solved for the spatially uniform semiconductors using a variety of well known techniques [26], but in a heterostructure, the crystal composition and/or strain varies from region to region and approximations are made in order to solve Eq. (2.2). Many such well known approximate methods are described in [27].

In our work, we use an 8 band $\mathbf{k}\cdot\mathbf{p}$ method [28]. So the wavefunctions take the form of Eq. (2.5). The summation is restricted to Bloch waves whose energies are close to the fundamental gap. Eight functions in the set are considered, namely the spin up and the spin down zone center Bloch waves from the s -like conduction band minimum, and spin up and spin down functions from each of the three degenerate p -like states at the top of the valence band. The Bloch waves are arranged in the following order: $|S \uparrow\rangle$, $|X \uparrow\rangle$, $|Y \uparrow\rangle$, $|Z \downarrow\rangle$, $|S \downarrow\rangle$, $|X \downarrow\rangle$, $|Y \downarrow\rangle$ and $|Z \downarrow\rangle$.

2.1.1 The Hamiltonian Matrix

The Hamiltonian matrix H takes the form [29].

$$H = \begin{bmatrix} G & \Gamma \\ -\Gamma^* & G^* \end{bmatrix} \quad (2.6)$$

Where G and Γ are both 4×4 matrix. Kané in [28] defined the matrix as follows:

$$G(\mathbf{k}) = G_1(\mathbf{k}) + G_2(\mathbf{k}) + G_{so}(\mathbf{k}). \quad (2.7)$$

Where

$$G_1 \equiv \begin{bmatrix} E_c & iPk_x & iPk_y & iPk_z \\ -iPk_x & E_{v'} & 0 & 0 \\ -iPk_y & 0 & E_{v'} & 0 \\ -iPk_z & 0 & 0 & E_{v'} \end{bmatrix} \quad (2.8)$$

$$G_2 \equiv \begin{bmatrix} A'k^2 & Bk_y k_z & Bk_x k_z & Bk_x k_y \\ Bk_y k_z & L'k_x^2 + M(k_y^2 + k_z^2) & N'k_x k_y & N'k_x k_z \\ Bk_x k_z & N'k_x k_y & L'k_y^2 + M(k_x^2 + k_z^2) & N'k_y k_z \\ Bk_x k_y & N'k_x k_z & N'k_y k_z & L'k_z^2 + M(k_x^2 + k_y^2) \end{bmatrix} \quad (2.9)$$

and

$$G_{so} \equiv -\frac{\Delta}{3} \begin{bmatrix} 0 & 0 & 0 & 0 \\ 0 & 0 & i & 0 \\ 0 & -i & 0 & 0 \\ 0 & 0 & 0 & 0 \end{bmatrix} \quad (2.10)$$

and the matrix Γ is

$$\Gamma \equiv -\frac{\Delta}{3} \begin{bmatrix} 0 & 0 & 0 & 0 \\ 0 & 0 & 0 & -1 \\ 0 & 0 & 0 & i \\ 0 & 1 & -i & 0 \end{bmatrix} \quad (2.11)$$

2.1.2 The Hamiltonian Matrix Elements

All the parameters appearing in Eq. (2.8)- (2.11) are real. The value of these parameters remain constant in each region. The parameters A' , B , L' , M , N' are defined by Kane [29] in terms of $\mathbf{k}\cdot\mathbf{p}$ theory. The Kane parameters may be given in terms of the Luttinger parameters [30].

$$\begin{aligned} L' &= -\frac{\hbar^2}{2m_0}(1 + \gamma_1 + 4\gamma_2) + \frac{P^2}{E_g} \\ M &= -\frac{\hbar^2}{2m_0}(1 + \gamma_1 - 2\gamma_2). \\ N' &= -\frac{3\hbar^2}{m_0}\gamma_3 + \frac{P^2}{E_g}. \end{aligned} \quad (2.12)$$

Where $E_g = E_c - E_v$ is the band edge gap with $E_v = E_{v'} + \Delta/3$. Δ is the spin orbit splitting parameter. The parameter P known, as the optical matrix element, is proportional to the momentum matrix element between the conduction band and the valence band.

$$P \equiv -i\frac{\hbar}{m_0}\langle s|p_x|x\rangle. \quad (2.13)$$

The Luttinger parameters are related to the effective masses in the following manner

$$\begin{aligned} \frac{m_0}{m_{hh}(100)} &= \gamma_1 - 2\gamma_2 & \frac{m_0}{m_{lh}(100)} &= \gamma_1 + 2\gamma_2 \\ \frac{m_0}{m_{hh}(111)} &= \gamma_1 - 2\gamma_3 & \frac{m_0}{m_{lh}(100)} &= \gamma_1 + 2\gamma_3. \end{aligned}$$

where $m_{hh(lh)}(ijk)$ is the heavy (light) hole effective mass in the (ijk) crystallographic direction.

2.2 Strain Analysis

It was originally suggested by Yablonovitch and Kane [8] and independently by Adams [9] that introduction of compressive strain into the crystal lattice of a semiconductor could lead to enhanced performance in semiconductor lasers. Strained layer buried heterostructure lasers are becoming increasingly important for optoelectronic applications, for example, in optical communication systems. The combination of strain and quantum confinement in the valence band can lead to substantially more favorable energy dispersion relationship than those that exist in the natural semiconductor crystal structure [31].

In semiconductors there exists a serious asymmetry between the very light conduction band and very heavy valence band effective mass. Ideally these should be as light as possible. And the technology of band structure engineering, which incorporates superlattice, confinement and intentional incorporation of strain can be used to change the band structure in an artificial manner to suit our needs.

2.2.1 Strain Effect on Electronic States

The 8×8 Hamiltonian matrix described in Eq. (2.6) - (2.11) using the 8 band $\mathbf{k}\cdot\mathbf{p}$ model, acquires extra terms when the crystal is under strain. This strain interaction couples only the parallel spin and hence this interaction adds an

additional term G_{strain} to the Hamiltonian in Eq. (2.6). The additional matrix is

$$G_{strain} \equiv \begin{bmatrix} a_c[e_{xx} + e_{yy} + e_{zz}] & b'e_{yz} - iP \sum_j e_{xj}k_j & b'e_{zx} - iP \sum_j e_{yj}k_j & b'e_{xy} - iP \sum_j e_{zj}k_j \\ b'e_{yz} - iP \sum_j e_{xj}k_j & le_{xx} + m(e_{yy} + e_{zz}) & ne_{xy} & ne_{zx} \\ b'e_{zx} - iP \sum_j e_{yj}k_j & ne_{xy} & le_{yy} + m(e_{xx} + e_{zz}) & ne_{yz} \\ b'e_{xy} - iP \sum_j e_{zj}k_j & ne_{xz} & ne_{yz} & le_{zz} + m(e_{xx} + e_{yy}) \end{bmatrix} \quad (2.14)$$

Where e_{ij} are the strained tensor components. The constants l , m and n are related to the material deformation potentials by:

$$a_v = \frac{1}{3}(l + 2m), \quad b_v = \frac{1}{3}(l - m) \quad \text{and} \quad d_v = \frac{1}{\sqrt{3}}n. \quad (2.15)$$

Where a_c is the conduction band hydrostatic deformation potential, a_v is the valence band hydrostatic deformation potential, b_v is the valence band shear deformation potential associated with stain along (100) crystallographic direction and d_v is the valence band shear deformation potential for stain along (111) crystallographic direction.

2.3 The Electron-Photon Interaction

In quantifying the gain or absorption, we need to know the number of transitions that will occur per second in the crystal in response to a given photon flux in a given optical mode. This is accomplished by studying the time evolution of a given electron wavefunction Ψ , initially in the conduction band state, ψ_e , as it makes a transition to the valence band or vice versa. The transition rate can be expressed using Fermi's Golden rule [32]

$$W_{e \rightarrow h} = \frac{2\pi}{\hbar} |H'_{eh}|^2 \delta(E_e - E_h - \hbar\omega). \quad (2.16)$$

Here H'_{eh} is given by

$$H'_{eh} \equiv \langle \psi_h | H'(r) | \psi_e \rangle. \quad (2.17)$$

Also it can be expressed as

$$|H'_{eh}|^2 = \left(\frac{eA_0}{2m_0} \right)^2 |M_T|^2. \quad (2.18)$$

Where A_0 is the magnitude of vector potential and M_T is the transition matrix element. Eq. (2.16) refers to only single transition pair over a continuum states. The correct transition rate is the summation of all the transition over all the continuum states.

2.4 The Gain/Absorption Spectrum

Eq. (2.16) allows us to determine the number of the downward transitions per second per unit volume in response to a flux of incoming photons in a given optical mode. Upward transitions or the absorption of the photons also occur in response to the incoming photon flux. Each downward transition

generates a new photon and each upward transition absorbs one. If the number of downwards transition per second exceeds the number of upward transition per second, then a net generation of photon occurs and optical gain can be achieved. If the opposite becomes true then the optical absorption occur.

The material gain g as a function of photon energy may be expressed as

$$g(\hbar\omega) = \left(\frac{1}{\hbar\omega}\right) \frac{\pi e^2 \hbar}{\varepsilon_0 c m_0^2 n} |M_T|^2 \rho_{red}(E_{ch} - E'_g)(f_c - f_v). \quad (2.19)$$

Where ρ_{red} is the reduced density of states, $f_c(f_v)$ is the electron (hole) occupation probability, and M_T is the transition matrix element for interband transitions.

The total gain for a particular photon energy in low-dimensional structures is found by summing over all subband transition pairs as:

$$g(\hbar\omega) = \sum_{n_c} \sum_{n_v} g_{sub}(\hbar\omega, n_c, n_v). \quad (2.20)$$

Where $g_{sub}(\hbar\omega, n_c, n_v)$ is denoted as the subband transition pair and n_c and n_v is the band index of the conduction and the valence band respectively. It is convenient to calculate the modal gain, g_{mod} in terms of g , the local gain in the active layers. This is the gain that would occur in a uniform active medium having the same optical properties. We can relate g to g_{mod} by

$$\frac{g_{mod}}{g} = \Gamma_{act}. \quad (2.21)$$

where Γ_{act} is known as the mode occupation factor of the active layers. For a QWire structure, considering the fact that not all regions within the active layer plane are active, g_{mod} and g are related by:

$$\frac{g_{mod}}{g} = \Gamma_{act} \frac{L_y}{L_P}. \quad (2.22)$$

where L_P is the period of the QWire arrangement along the in-plane direction and L_y is the width of the QWire along the in-plane direction. From Eq. (2.16) we can see that when $f_c(E_c) > f_c(E_v)$, then $g(\hbar\omega)$ is positive and an incoming light wave with photon energy $\hbar\omega$ will be amplified by the material. Whereas If the electron carrier density is small, then f_c will be close to zero and hence the gain will be negative. And at this condition the material is highly absorbing for photon energies greater than the band gap.

Chapter 3

Calculation Procedure

In this chapter the procedures of our numeric calculations are described.

3.1 Material Properties of GaInAsP/InP Systems

Fig. 3.1 shows the schematic diagram of the device structure and Fig. 3.2 shows the cross-sectional diagram of the unit cell of the GaInAsP vertically stacked multiple QWire EAM under our consideration. The device structure consists of quaternary $\text{Ga}_x\text{In}_{(1-x)}\text{As}_y\text{P}_{(1-y)}$ grown on an (001) InP substrate. The wire regions are compressively strained and the barriers are either lattice matched (LM) to InP or are tensile strained (TS).

3.1.1 Interpolation of Material Constant

The material constants can be found by interpolating from the known constants of alloys of given compositions. Material constants of the quaternaries are in general functions of their composition x and y . All the material constants for the quaternary are linearly interpolated between these of InP,

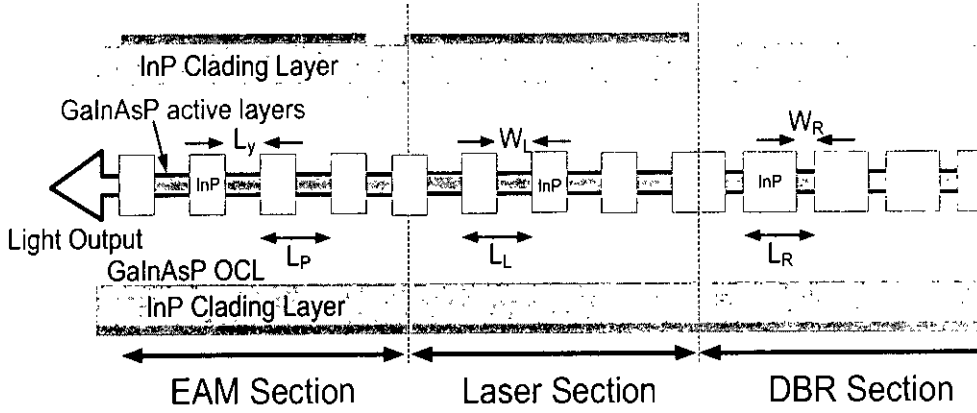


Figure 3.1: Schematic structure of a QWire EAM integrated with QWire laser and and Distributed Bragg Reflector sections.

GaAs, InAs and the LM ternary $\text{Ga}_{0.468}\text{In}_{0.532}\text{As}$ assuming Vegard's law [33].

$$A^Q(x, y) = (1 - y)A^{\text{InP}} + yA^T + y(A^{\text{GaAs}} - A^{\text{InAs}})(x - 0.468y). \quad (3.1)$$

Where A is one of the material constants, Q stands for the quaternary, T for the lattice matched ternary. The material parameters of the binary and ternary semiconductors are listed in Table. 3.1. For the quaternary band gap we use parabolic interpolation, to account for the bowing of the bandgap up to the second order [34].

$$E_g^Q(x, y) = E_g^{\text{InP}} + 0.672x - 1.091y + 0.758x^2 + 0.101y^2 + 0.111xy - 0.580x^2y - 0.159xy^2 + 0.268x^2y^2. \quad (3.2)$$

The following interpolation formula was used for the determination of lattice constants:

$$a^Q(x, y) = a^{\text{InP}} + 0.189y - 0.418x + 0.013xy. \quad (3.3)$$

The lattice mismatch strain, ϵ_0 and it is defined by:

$$\epsilon_0 = \frac{a^{\text{InP}} - a^Q}{a^Q}. \quad (3.4)$$

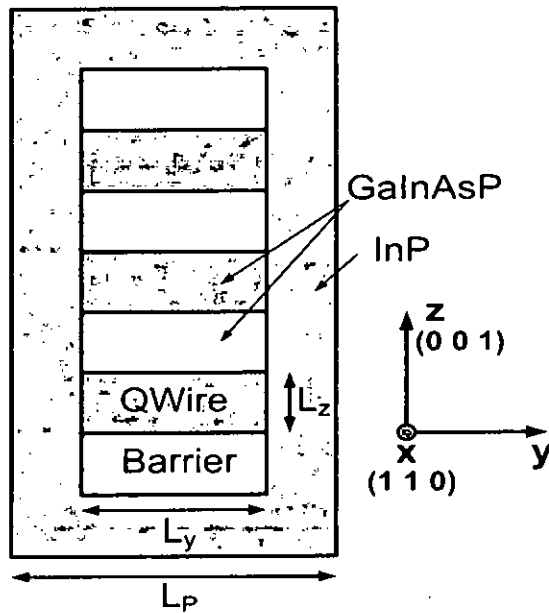


Figure 3.2: Cross-sectional schematic diagram of a vertical stack of multiple QWire structures.

3.2 Analytical Expressions for Strain Distribution

We follow an analytical method for calculating strain distributions in structures containing an arbitrary number and combination of strained layers of finite width buried in an infinite layer as described in [35]. The materials are assumed to be continuous, linear and isotropic obeying Hooke's laws.

Fig. (3.3) represents a single strained layer of width L_y and thickness L_z buried in an infinite medium. The misfit strain is ϵ_0 within the QWire and zero outside. The dimension of the structure in x direction is assumed to be

Table 3.1: Material Constant

Constants	GaAs	InAs	InP	In _{0.532} Ga _{0.468} As
$E_g(300K)$ eV	1.424	0.354	1.351	0.75
Δ_0 eV	0.341	0.371	0.110	0.356
m_e^*/m_0	0.0665	0.023	0.079	0.041
γ_1	6.790	19.67	4.95	11.01
γ_2	1.924	8.37	1.65	4.18
γ_3	2.782	9.29	2.35	4.84
a_g (eV)	-9.77	-6.0	-6.35	-7.76
a_c (eV)	-7.1	-5.4	-5.35	-6.2
b_v (eV)	-1.7	-1.8	-2.0	-1.75
d_v (eV)	-4.55	-3.6	-4.2	-4.04
E_p (eV)	28.8	22.2	20.4	25.3
$C_{11}(\times 10^{11}$ dyn/cm ²)	11.81	8.329	10.22	10.08
$C_{12}(\times 10^{11}$ dyn/cm ²)	5.38	4.53	5.76	4.98
$C_{14}(\times 10^{11}$ dyn/cm ²)	5.94	3.96	4.60	4.89
a (300K) Å	5.6532	6.0583	5.8587	5.8687

very large (ideally infinite) compared to L_y or L_z so that a two-dimensional analysis with plane strain condition is appropriate. The analysis starts with the solution of a cylindrical inclusion. The cylindrical inclusion of radius r exerting a pressure S yields stress fields outside the cylinder which are easily determined [35]. Dividing the stresses by πr^2 give the stress components per unit area of inclusion:

$$\sigma_{yy}^{cyl} = \frac{S}{\pi} \frac{y^2 - z^2}{(y^2 + z^2)^2},$$

$$\sigma_{zz}^{cyl} = \frac{S}{\pi} \frac{z^2 - y^2}{(y^2 + z^2)^2}, \quad (3.5)$$

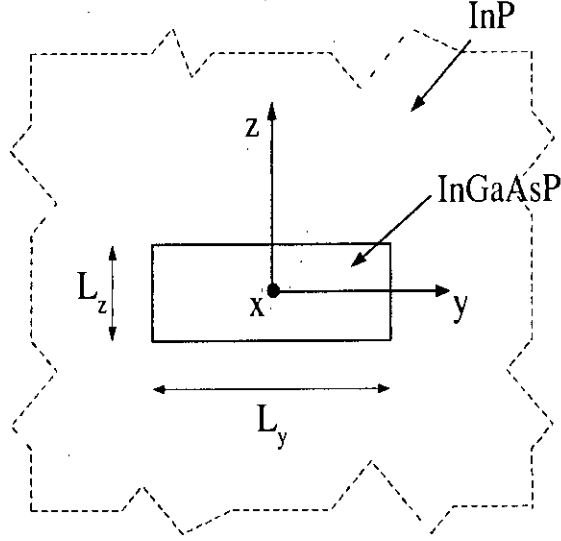


Figure 3.3: Cross-sectional schematic diagram of a strained QWire structure.

$$\sigma_{yz}^{cyl} = \frac{2S}{\pi} \frac{yz}{(y^2 + z^2)^2}.$$

The stress fields for the n th strained layer illustrated in Fig. 3.2 are obtained by integrating the stress field over a rectangle of width L_y and height L_z , thus

$$\sigma^n(y, z) = \int_{(L_y)} \int_{(L_z)} \sigma^{cyl}(y - y_0, z - z_0) dz_0 dy_0. \quad (3.6)$$

Generating the results,

$$\begin{aligned} \sigma_{yy}^n(y, z) &= \frac{S}{\pi} \left[\tan^{-1} \left(\frac{l_y - y}{l_z - z} \right) + \tan^{-1} \left(\frac{l_y + y}{l_z - z} \right) \right. \\ &\quad \left. + \tan^{-1} \left(\frac{l_y - y}{l_z + z} \right) + \tan^{-1} \left(\frac{l_y + y}{l_z + z} \right) \right], \\ \sigma_{zz}^n(y, z) &= \frac{S}{\pi} \left[\tan^{-1} \left(\frac{l_z - z}{l_y - y} \right) + \tan^{-1} \left(\frac{l_z + z}{l_y - y} \right) \right. \\ &\quad \left. + \tan^{-1} \left(\frac{l_z - z}{l_y + y} \right) + \tan^{-1} \left(\frac{l_z + z}{l_y + y} \right) \right]. \quad (3.7) \end{aligned}$$

$$\begin{aligned}\sigma_{yz}^n(y, z) &= \frac{S}{2\pi} \left[\ln|(l_y + y)^2 + (l_z - z)^2| + \ln|(l_y - y)^2 + (l_z + z)^2| \right. \\ &\quad \left. - \ln|(l_y - y)^2 + (l_z - z)^2| - \ln|(l_y + y)^2 + (l_z + z)^2| \right]\end{aligned}$$

These are the stress fields associated with a single strained layer of dimension $L_y \times L_z$ buried in an infinite medium where $2l_y = L_y$ and $2l_z = L_z$. The principle of superposition is used to calculate the stress field at a point due to many strained layer. The stress field component given in Eq. (3.7) are used to determine the strain components using Hooke's laws. Here, ϵ_{xxx} is equal to the misfit strain ϵ_0 , within the strained layer, but ϵ_{xxx} is equal to zero outside this region. The Hooke's law relations for plane strain for the n th strained layer, therefore, become [35]

$$\begin{aligned}\epsilon_{yy}^n(y, z) &= \frac{1}{E} \left[(1 - \nu^2)\sigma_{yy}^n - \nu(1 + \nu)\sigma_{zz}^n \right] - \nu\epsilon_0(y, z), \\ \epsilon_{zz}^n(y, z) &= \frac{1}{E} \left[(1 - \nu^2)\sigma_{zz}^n - \nu(1 + \nu)\sigma_{yy}^n \right] - \nu\epsilon_0(y, z),\end{aligned}\quad (3.8)$$

$$\epsilon_{yz}^n(y, z) = \frac{2(1 + \nu)}{E}\sigma_{yz}^n$$

Where $\epsilon_0(y, z)$ is the misfit of the material at position (y, z) , E is the Young's modulus and ν is the Poisson's ratio. Equations (3.7) give the in-plane stress at the center of a long thin layer ($L_y/L_z \rightarrow \infty$) as $2S$. The Hooke's law expression then yields

$$S = \frac{\epsilon_0 E}{2(1 - \nu)}\quad (3.9)$$

3.3 Electronic States of Semiconductor Heterostructures

The heterostructure is composed of several regions, each of a definite composition and/or uniform state of strain. In such a situation, the parameters in the Hamiltonian matrix defined in Eq. (2.6) are constant in each region but differ from region to region. The envelope functions of one region must match those of the next region. A simple prescription for automatically including the correct boundary conditions into the formulation of the problem was studied in [36]. According that prescription, every term of Eq. (2.8) and Eq. (2.9) in which both a material parameter and a derivative appear, is replaced in the following way.

$$Q \frac{\partial}{\partial x_\mu} \rightarrow \frac{1}{2} \left[Q(\mathbf{r}) \frac{\partial}{\partial x_\mu} + \frac{\partial}{\partial x_\mu} Q(\mathbf{r}) \right],$$

$$Q \frac{\partial}{\partial x_\mu} \frac{\partial}{\partial x_\nu} \rightarrow \frac{1}{2} \left[\frac{\partial}{\partial x_\mu} Q(\mathbf{r}) \frac{\partial}{\partial x_\nu} + \frac{\partial}{\partial x_\nu} Q(\mathbf{r}) \frac{\partial}{\partial x_\mu} \right]. \quad (3.10)$$

where $Q(\mathbf{r})$ is any real material parameter or strain tensor component. The spatial dependence of the parameter $Q(\mathbf{r})$ is expressed in terms of step functions at the interfaces i.e., for an interface $x = x_0$, where material A is to the left side of the interface and B is to the right side:

$$Q(x) = Q_A + (Q_B - Q_A)\Theta(x - x_0). \quad (3.11)$$

Where the step function Θ is defined as

$$\Theta(x - x_0) = \begin{cases} 0, & x < x_0 \\ 1, & x \geq x_0 \end{cases} \quad (3.12)$$

The derivative operator on the step function produces the delta function which impose the correct slope discontinuity boundary condition on a solution which is treated as being continuous. The delta function is to be retained in the elements of the Hamiltonian matrix. The 8×8 matrix obtained in this way has elements $H_{nn'}(\mathbf{r}, \nabla)$ and eight coupled differential equations are:

$$\sum_{n'=1}^8 H_{nn'}(\mathbf{r}, \nabla) F_n'(\mathbf{r}) = E F_n(\mathbf{r}) \quad (3.13)$$

These equations can be solved by the eigenfunction expansion method [36]. In the case of QWire structures the envelope function F_n , for a particular wavevector k_x along the QWire axis is expressed in terms of a two dimensional Fourier series as:

$$F_n(\mathbf{r}) = \sum_{lm}^{\infty} F_n(k_x, l, m) \phi_{k_x, lm}(xyz). \quad (3.14)$$

Where the basis function ϕ is

$$\phi_{k_x, lm}(xyz) = \frac{1}{\sqrt{L_y L_z}} \exp \left[i k_x x + 2\pi i \left(l \frac{y}{L_y} + m \frac{z}{L_z} \right) \right]. \quad (3.15)$$

In order to convert Eq. (3.13) into a set of algebraic equations, we insert Eq. (3.14) into Eq. (3.13), multiply by $\phi_{lmk_x}^*(xyz)$ and integrate over the region $L_y L_z$. The resultant matrix eigenvalue equation has the form:

$$\sum_{n'l'm'} H_{nn'}(l', m', l, m) F_n'(l', m') = E F_n(l, m), \quad (3.16)$$

Where the matrix elements $H_{nn'}(l', m', l, m)$ are given by:

$$H_{nn'}(l', m', l, m) = \int dy dz \phi_{l'm'}^*(yz) H_{nn'}(\mathbf{r}, \nabla) \phi_{lm}(yz) \quad (3.17)$$

All the matrix elements can be evaluated analytically for each interface perpendicular to one or another co-ordinate axis. For the QWire structure the

matrix element in Eq. (3.17) is given by

$$H_{nm'}(l', m', l, m, k_x) = \int_{L_y} \int_{L_z} dy dz \phi_{l'm'}^*(yz) H_{nm'}(y, z, k_x, \frac{\partial}{\partial y}, \frac{\partial}{\partial z}) \phi_{lm}(yz). \quad (3.18)$$

Solution of Eq. (3.16) for given k_x gives the eigenenergy E and the coefficients of the envelope function $F_n(l, m)$.

We solved the heterostructure problem by diagonalizing the large Hamiltonian matrix $H_{nm'}(l', m', l, m)$ as given in Eq. (3.17) and Eq. (3.18). This matrix is complex and Hermitian. The matrix elements can be obtained by solving the integral, extend over all spatial regions. For the QWire case the bulk contributions to the matrix elements contain integrals of the form:

$$I_{l', m', l, m}^R = \frac{1}{L_y L_z} \int_{R_{L_y}}^{R_{R_y}} \int_{R_{L_z}}^{R_{R_z}} dy dz e^{-i(l' \frac{y}{L_y} + m' \frac{z}{L_z})} e^{i(l \frac{y}{L_y} + m \frac{z}{L_z})}. \quad (3.19)$$

where R_{L_y} , R_{L_z} are the left side edges of the zone R along y , z directions, respectively and R_{R_y} , R_{R_z} are its right side edges along the same directions. Analytical solutions for these integral for the QWire structure are,

$$I_{l', m', l, m}^R = \begin{cases} \frac{1}{L_y L_z} (R_{R_y} - R_{L_y})(R_{R_z} - R_{L_z}) & ; l = l', m = m' \\ \frac{1}{i L_y L_z} \left[\frac{L_y}{l-l'} \left(e^{i \frac{l-l'}{L_y} R_{R_y}} - e^{i \frac{l-l'}{L_y} R_{L_y}} \right) \right] + \\ \frac{1}{i L_y L_z} \left[\frac{L_z}{m-m'} \left(e^{i \frac{m-m'}{L_z} R_{R_z}} - e^{i \frac{m-m'}{L_z} R_{L_z}} \right) \right] & ; l \neq l', m \neq m' \end{cases} \quad (3.20)$$

After completing the construction of the matrix elements for QWire, they are diagonalized to get the eigenenergies E .

3.4 Transition Matrix Elements

For evaluating the transition rate between the initial state $\Psi_i(\mathbf{r})$ and the final state $\Psi_f(\mathbf{r})$ of carriers, we calculated the term:

$$|\langle \Psi_f(\mathbf{r}) | H_{rad} | \Psi_i(\mathbf{r}) \rangle|^2 = \mathbf{A}_0^2 \left(\frac{e}{2m_0c} \right)^2 M_{f,i}. \quad (3.21)$$

Where $M_{f,i}$ is known as the optical matrix element and it is given by [29]:

$$M_{f,i} = |\langle \psi_f(\mathbf{r}) | \hat{\mathbf{e}} \cdot \frac{\hbar}{i} \nabla | \psi_i(\mathbf{r}) \rangle|^2. \quad (3.22)$$

Where $\hat{\mathbf{e}}$ is a unit vector in the direction of the electric field of the radiation. States i and f may both belong to the valence band or conduction band for either of the inter-band and intra-band transition. Now, substituting

$$\begin{aligned} \psi_{i,f}(\mathbf{r}) &= \sum_{n=1}^8 F_n^{i,f}(\mathbf{r}) U_n(\mathbf{r}) \\ &= \sum_{n=1}^8 \sum_{jlm} F_n^{i,f}(j, l, m) \phi_{jlm}(xyz) U_n(\mathbf{r}). \end{aligned} \quad (3.23)$$

into Eq. (3.22)

$$\begin{aligned} M_{f,i} &= \left| \sum_{n,n'=1}^8 \sum_{jlm} \sum_{j'l'm'} F_n^{f*}(j, l, m) F_{n'}^i(j', l', m') \right. \\ &\quad \left. \int \phi_{jlm}^* U_n^*(\mathbf{r}) \hat{\mathbf{e}} \cdot \frac{\hbar}{i} \nabla \phi_{j'l'm'}(xyz) U_{n'}(\mathbf{r}) dx dy dz dr \right|^2. \end{aligned} \quad (3.24)$$

Assuming the envelope functions vary relatively slow over regions the size of a unit cell, we can write the integral in the Eq. (3.24) as

$$\begin{aligned} &\int \phi_{jlm}^*(xyz) U_n^*(\mathbf{r}) \hat{\mathbf{e}} \cdot \nabla \phi_{j'l'm'}(xyz) U_{n'}(\mathbf{r}) dr dx dy dz \\ &\cong \int \phi_{jlm}^*(xyz) \phi_{j'l'm'}(xyz) dx dy dz \end{aligned}$$

$$\begin{aligned}
& \int_{\Omega(xyz)} U_n^*(\mathbf{r}) \hat{\mathbf{e}} \cdot \nabla U_{n'}(\mathbf{r}) d\mathbf{r} \\
& + \int \phi_{jlm}^*(xyz) \hat{\mathbf{e}} \cdot \nabla \phi_{j'l'm'}^*(xyz) dx dy dz \\
& \int_{\Omega(xyz)} U_n^*(\mathbf{r}) U_{n'}(\mathbf{r}) d\mathbf{r}. \tag{3.25}
\end{aligned}$$

The first integral over $\Omega(xyz)$ in Eq. (3.25) is actually a sum of three integrals, each being multiplied by a component of $\hat{\mathbf{e}}$. Each of the three is proportional to the optical matrix P or else vanishes unless n, n' and the component of ∇ are related in a way such that both n and n' must refer to the same direction of spin, n must be in the conduction band while n' must be in the valence band or vice versa. The second integral over $\Omega(xyz)$ is the overlap of two Bloch waves. It vanishes unless $n = n'$.

3.5 The Gain/Absorption Spectra

In order to calculate the gain/absorption spectra we have to evaluate Eq. (2.19). For that we first compute the band structure associated with the QWire. For a given carrier density the quasi Fermi energies are calculated according to [32]. The reduced density-of-states (RDOS) can also be determined from the bandstructure.

$$\text{RDOS} = \left[\frac{\rho(k)}{dE_{ch}/dk} \right]_{E_{ch}=\hbar\omega} \tag{3.26}$$

Where $E_{ch} \equiv E_e - E_h$ is the transition energy and ρ is the density of states. Once these quantities are evaluated, the gain/absorption spectra can be evaluated in a straight forward way.

Interactions of electrons with phonons and other electrons time to time scatter the electron into another conduction band state. Therefore, the lifetime of a given state is not infinite. It is presently believed that, on an

average, approximately every 0.1 ps an electron (or hole) is bumped into a new state [37]. Hence the energy of each state (and each transition) is no longer sharp but has an energy spread over a range of $\Delta E \approx \hbar/0.1 \text{ ps} \approx 7 \text{ meV}$ on each side of the expected energy of the state (or transition).

To include the spectral broadening of each transition, we convolve the expression for material gain with some spectral lineshape function over all transition energies E_{eh} to obtain [32],

$$G(\hbar\omega) \equiv \int g(\hbar\omega) L(E_{eh}) dE_{eh}. \quad (3.27)$$

Where

$$L(E_{eh}) \equiv \frac{1}{\pi} \frac{\hbar/\tau_{in}}{(E_{eh} - \hbar\omega)^2 + (\hbar/\tau_{in})^2}. \quad (3.28)$$

Where $g(\hbar\omega)$ is taken directly from Eq. (2.19), $L(E_{eh})$ is a normalized Lorentzian lineshape function, and τ_{in} is the intra-band relaxation time or simply the lifetime of each state, and it is about 0.1ps in bulk material [32].

3.6 Bandgap Reduction Due to Application of Electric Field

In undoped materials the main photoluminescence (PL) properties has been attributed to the transition between the ground levels of the conduction and the valence band. Under the influence of applied electric field, applied perpendicularly, significant effects on the carrier confinement and energy states of the QWire and QWell occur.

The Hamiltonian matrix elements in Eq. (2.8) in the presence of an electric field along the z direction becomes

$$G_1 \equiv \begin{bmatrix} E_c + zF_s & iPk_x & iPk_y & iPk_z \\ -iPk_x & E_{v'} + zF_s & 0 & 0 \\ -iPk_y & 0 & E_{v'} + zF_s & 0 \\ -iPk_z & 0 & 0 & E_{v'} + zF_s \end{bmatrix}. \quad (3.29)$$

The extra term in the diagonal elements gives rise to additional terms in the diagonal elements of Eq. (3.17). These terms may also be evaluated analytically and the formulation of section 3.3 is allied with this modification. Where F_s is the applied electric field per unit length of the device.

3.7 Calculation of Extinction Ratio

Extinction ratio (ER), which express the efficiency of a modulator, can be expressed as the ratio of two optical power levels (P_1/P_2), of a digital signal generated by an optical source, i.e., a laser diode. Here P_1 is the output optical power level when the modulator is *on*, and P_2 is the power level when the modulator is *off*. Normally extinction ratio is expressed in dB. We have used the relationship of extinction ratio followed in [38].

$$\text{ER} = 10 \log \frac{P_{out}(V)}{P_{out}(V=0)} \quad (3.30)$$

In our calculation the voltage V is a typical applied electric field of 125 KV/cm. Also the normalized level of output power in Eq. (3.30) is expressed as:

$$P_{out} = P_0 \exp(-\alpha_{abs} \Gamma L D) \quad (3.31)$$

Where P_0 is the intensity of the light incident on the modulator. α_{abs} is the absorption coefficient, Γ is the optical confinement factor of the initial wafer,

L is the total length of the device and $D = L_y/L_P$ is the in-plane filling factor.

Chapter 4

Results and Discussion

In this chapter, the results of the numerical calculation of QWire and QWell devices are presented. The device structure is shown in the Fig. (3.2). The initial wafer consists of multiple layers of $\text{Ga}_x\text{In}_{1-x}\text{As}_y\text{P}_{1-y}$ biaxially CS quantum well layers. We use 1.07% compressive strain as the misfit strain in the QWire active region of our calculation. Different types of barriers used are LM and TS (0.15 %, 0.30 % and 0.60 %) grown on (001) InP substrate. In all our analysis the thickness of the well $L_z=7$ nm in the crystal growth direction and the thickness of the barriers is 12 nm unless otherwise mentioned.

4.1 Electronic States of QWires EAMs

The dispersion relationships of the lowest two conduction and the highest three valence band energy levels in 20 nm and 30 nm wide QWires are presented in Fig. 4.1 (a-b) and (c-d), respectively. The calculation procedures for the dispersion relationships of the QWires are presented in Section 3.3. LM and 0.15% TS barriers with single QWire stack (1S) structures are considered.

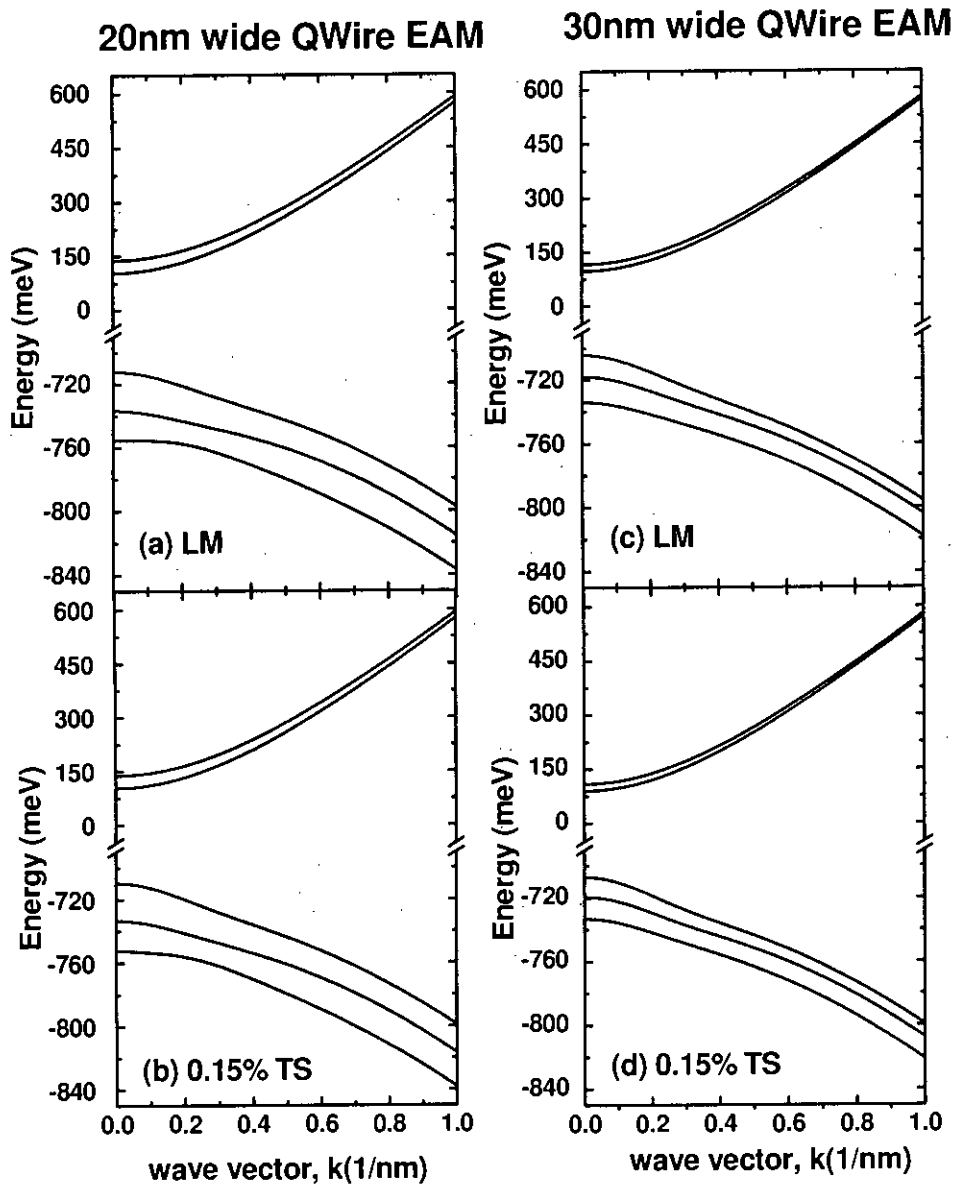


Figure 4.1: Dispersion relationships for the lowest two conduction and highest three valence band energy levels for 20 nm wide QWire EAMs (a)-(b) and 30 nm wide QWire (c)-(d) calculated for two different types of barriers.

It is found that for LM barriers, the nonparabolicity of the highest hole subband is strong near the zone centre due to band mixing. We also note that the band mixing in the excited hole subbands is stronger in the narrower QWire. Table 4.1 lists the values of the zone-centre effective mass of the highest hole sub band m_{h1} , zone-centre separation between the highest two hole subbands ΔE_{h12} , and the fundamental electron-hole transition energy E_0 for three QWires extracted from numerical data.

Table 4.1: Comparison of key dispersion relationship parameters for 10 nm, 20 nm, and 30 nm QWires

	LM Barriers			0.15% TS Barriers			0.6% TS Barriers		
	10 nm	20 nm	30 nm	10 nm	20 nm	30 nm	10 nm	20 nm	30 nm
m_{h1}/m_0	0.2708	0.1854	0.1604	0.2060	0.1564	0.1392	0.1247	0.1053	0.0982
$\Delta E_{h12}(\text{meV})$	28.49	26.54	14.40	28.99	25.27	13.90	30.73	21.97	12.41
$E_0(\text{meV})$	865.53	820.36	807.97	862.89	817.79	805.39	851.70	806.56	794.34

4.2 Effect of Electric Field on Band Structure of QWire EAMs

The dispersion relationships of the lowest conduction and the highest three valence band energy levels in 20 nm and 30 nm wide QWires for both with and without an applied electric field are presented in Fig. 4.2 (a-b) and (c-d), respectively. LM and 0.15% TS barriers with 1S structures are considered. A typical value of 125 KV/cm is used as the magnitude of the applied electric field. The conduction band levels are shifted downward and the valence band

levels are shifted upward in response to the field along the growth direction. This shift causes a reduction of the effective bandgap E_g . This bandgap reduction continues with the increase of the electric field. Fig. 4.3 shows the reduction of the bandgap with the electric field in 10 nm, 30 nm and 50 nm QWire EAMs. LM and 0.15% TS barriers with 1S structures are considered.

From Fig. 4.3, it is observed that the effect of the electric field on the effective bandgap E_g is parabolic. Therefore we propose a second order empirical relationship to relate the two quantities.

$$E_g = a - bF_S^2 \quad (4.1)$$

where F_S represent the applied electric field. Coefficients a and b in Eq. (4.1) are calculated from a fifth order polynomial function of the width L_y of the QWires.

$$\begin{aligned} a &= p_{5a}L_y^5 + p_{4a}L_y^4 + p_{3a}L_y^3 + p_{2a}L_y^2 + p_{1a}L_y + p_{0a} \\ b &= p_{5b}L_y^5 + p_{4b}L_y^4 + p_{3b}L_y^3 + p_{2b}L_y^2 + p_{1b}L_y + p_{0b} \end{aligned} \quad (4.2)$$

The values of the polynomial coefficients of Eq. (4.2) for CS QWires with 1.07% misfit strain are given in Table. 4.2. These are obtained by comparing with numerical results calculated from 8 band $\mathbf{k} \cdot \mathbf{p}$ model. Fifth order polynomial function is used in order to compromise between the amount of error and complexity in finding coefficients. In this case the maximum amount of error is less than 2 meV.

Fig. 4.4 shows E_g versus F_S for a number of QWires using Eq. (4.1) and Eq. (4.2) as well as numerical results. LM barriers are considered. The proposed empirical relationship predicts the bandgap reduction with the applied electric field accurately. Bandstructures of the devices under

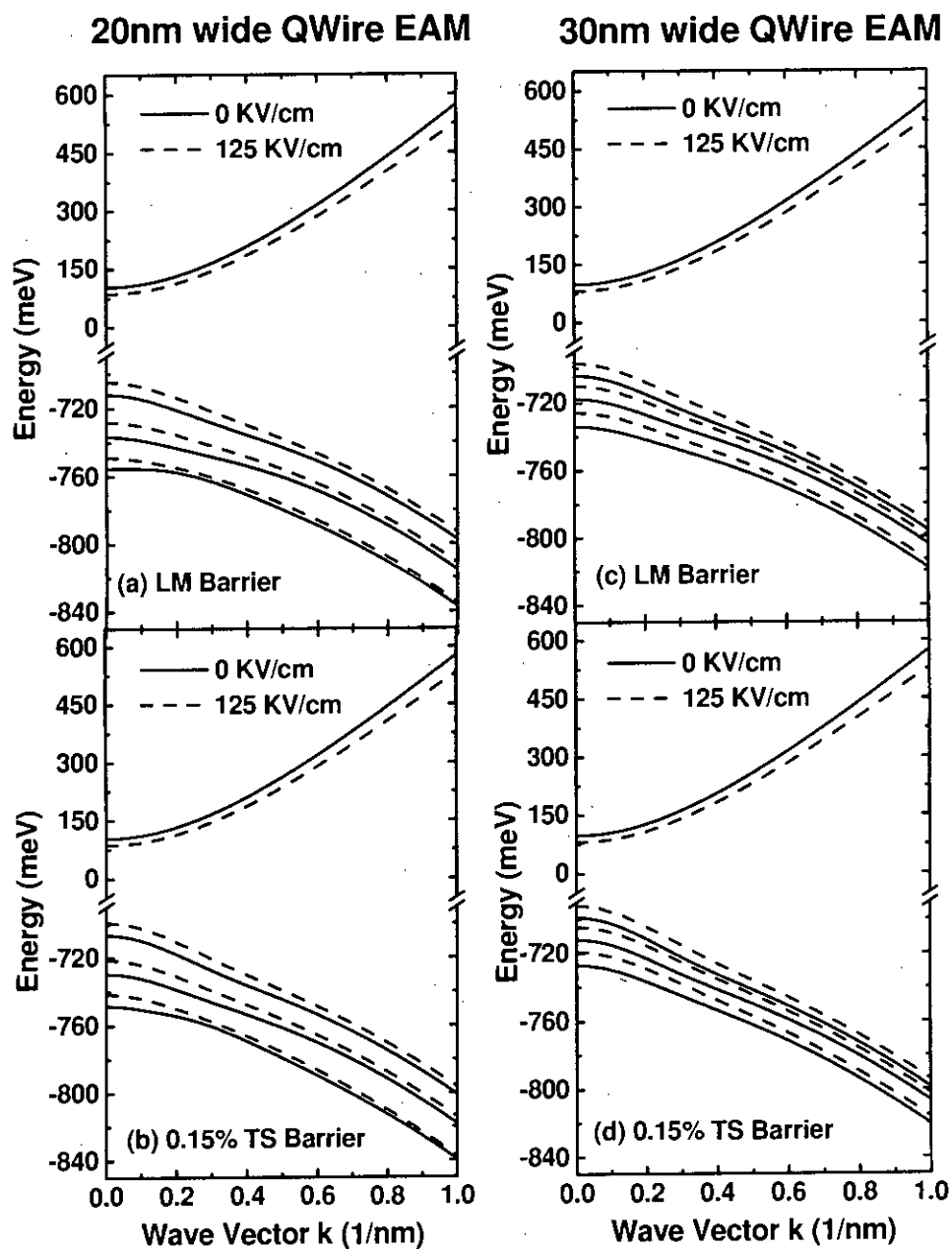


Figure 4.2: Dispersion relationships for the lowest conduction and the highest three valence band energy levels for 20 nm wide QWire (a-b) and 30 nm wide QWire (c-d) calculated for both zero and 125 KV/cm electric field. Two different types of barriers are considered.

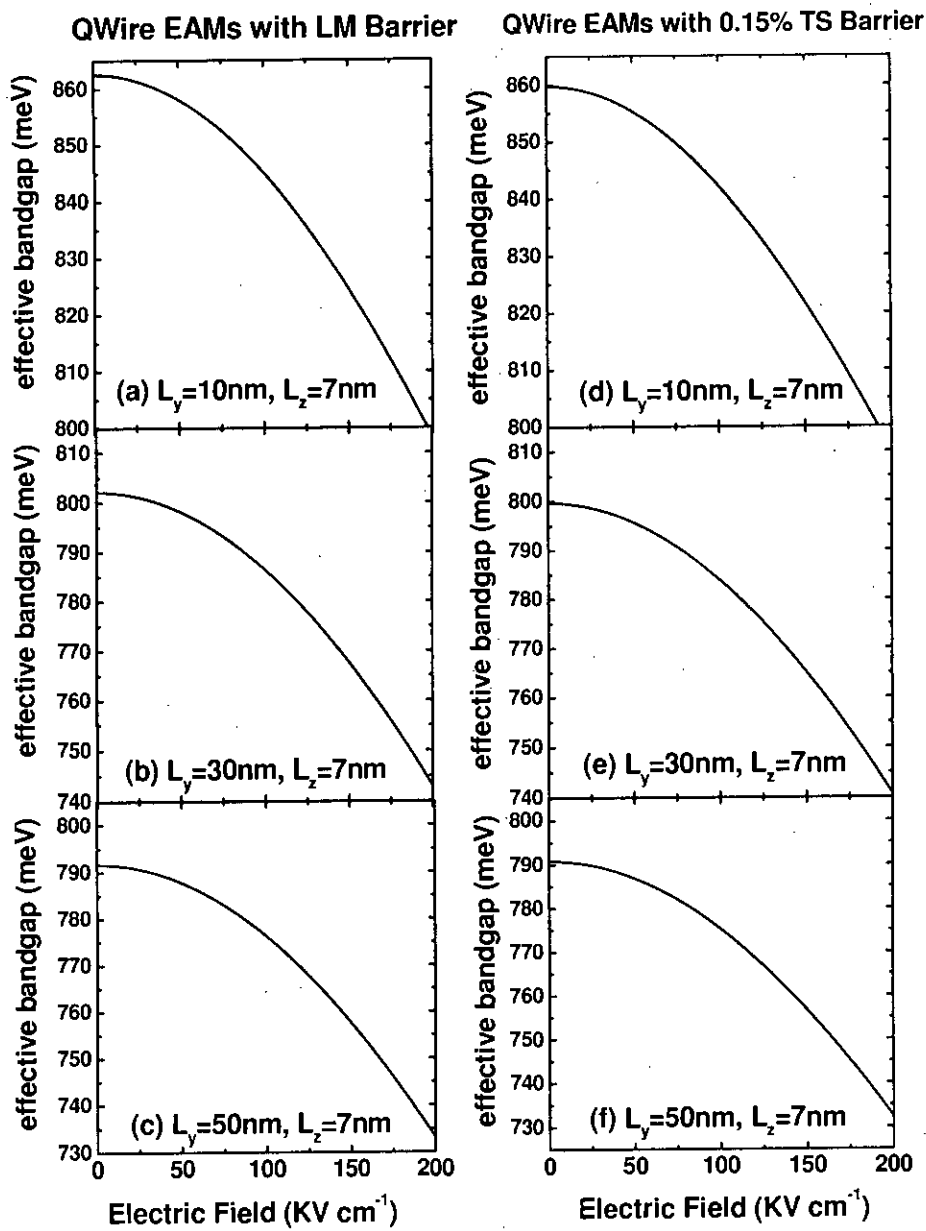


Figure 4.3: Electric field dependence of effective bandgap in 10 nm, 30 nm and 50 nm wide QWire EAMs for LM (a-c) and 0.15% TS (d-f) barriers. Single stack structures are considered.

Table 4.2: Coefficients of the Eq. (4.2) for the variable a and b of Eq. (4.1)

coefficient	P_{5a} (eV/nm ⁵)	P_{4a} (eV/nm ⁴)	P_{3a} (eV/nm ³)	P_{2a} (eV/nm ²)	P_{1a} (eV/nm)	P_{0a} (eV)
a	-2.94×10^{-9}	5.45×10^{-7}	-4.0×10^{-5}	1.47×10^{-3}	-2.809×10^{-2}	1.031
coefficient	P_{5b} (eVnm ⁻³ /V ²)	P_{4b} (eVnm ⁻² /V ²)	P_{3b} (eVnm ⁻¹ /V ²)	P_{2b} (eV/V ²)	P_{1b} (eVnm/V ²)	P_{0b} (eVnm ² /V ²)
b	-1.94×10^6	3.10×10^8	-1.95×10^{10}	6.12×10^{11}	-9.88×10^{12}	2.17×10^{14}

our consideration depend in addition to the width of the QWires, on the barrier strain compensation and on the height of the QWires. For accurately predicting the bandgap reduction with different amount of barrier strain compensation and QWire height, we modify the zeroth order terms in Eq. (4.2) in the following way.

$$\begin{aligned}
 P_{0a} &\longrightarrow P_{0a} - 0.015\xi + 0.006(7 - L_z) \\
 P_{0b} &\longrightarrow P_{0b} - 0.000025(7 - L_z).
 \end{aligned}
 \tag{4.3}$$

where ξ is the percent amount of tensile strain in the barrier region and L_z is the height of the QWires in nm. Eq. (4.3) incorporates the effect of barrier strain compensation and the wire height in the prediction function.

Fig. 4.5 shows the comparison of Eqs. (4.2) and (4.3) with numerical calculations for 10 nm, 30 nm and 50 nm QWire for 0.15% and 0.30% TS strained barriers. Fig. 4.6 shows the comparison for 10 nm, 30 nm, 50 nm QWire EAMs for different values of L_z . LM and 0.15% TS barriers are considered. It is evident from Figs. 4.4 - 4.6 that Eqs. (4.1) - (4.3) predicts the bandgap dependence of the QWires for different device conditions

QWire EAMs with LM Barriers

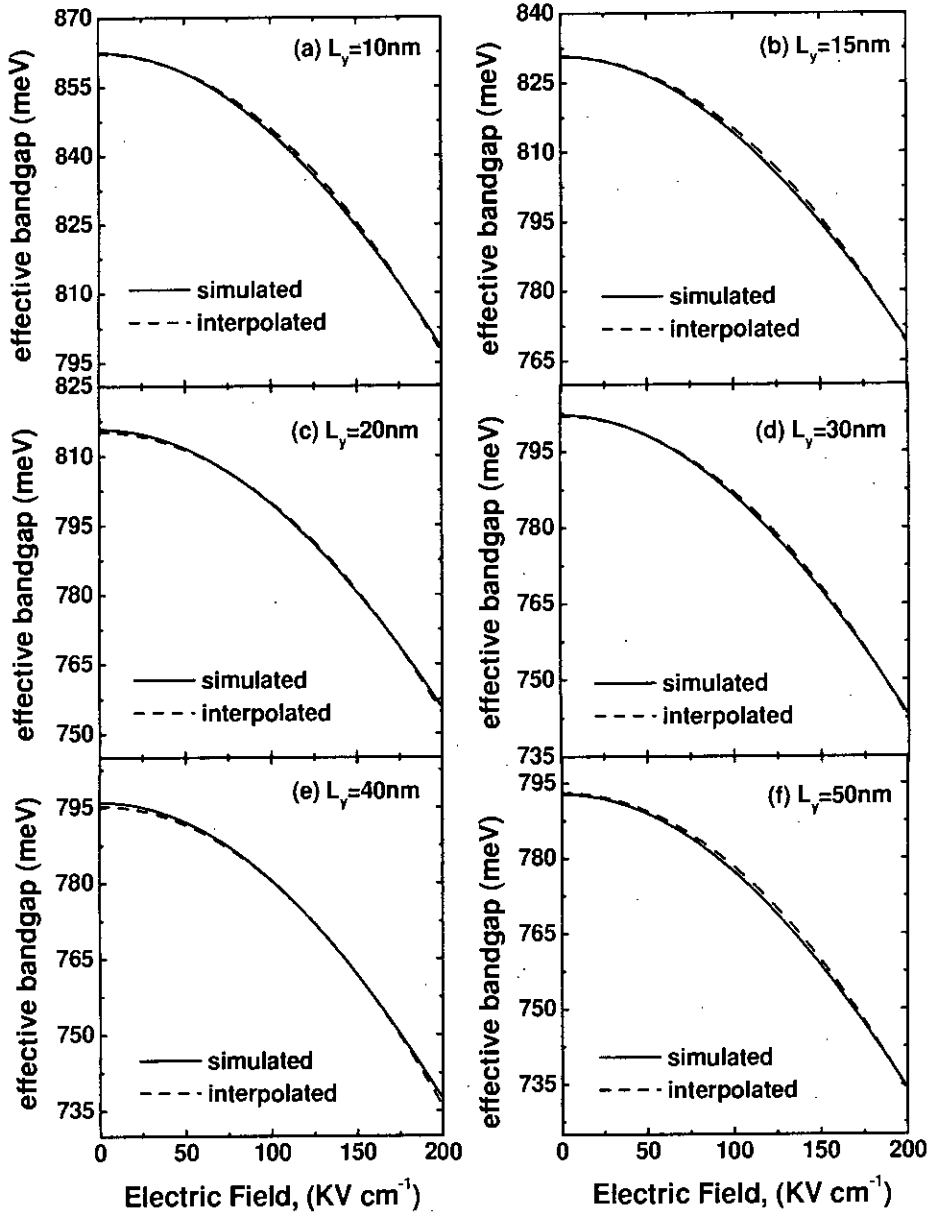


Figure 4.4: Electric field dependence of effective bandgap in 10 nm, 15 nm, 20 nm, 30 nm, 40 nm and 50 nm wide QWire EAMs for LM barrier calculated using the numerical method and Eqs. (4.1)-(4.3).

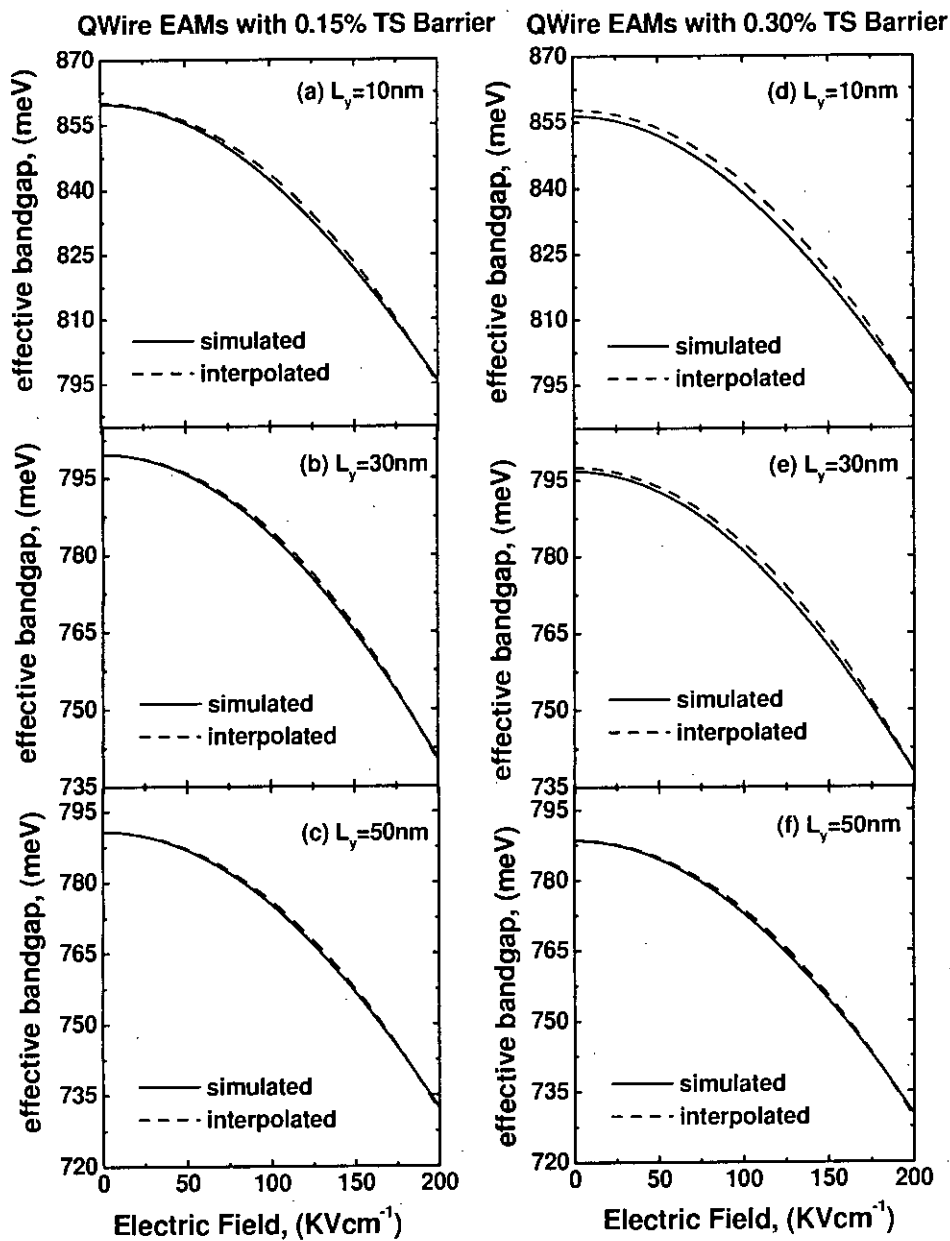


Figure 4.5: Electric field dependence of the effective bandgap in 10 nm, 30 nm, 50 nm for 0.15% TS barrier (a)-(c) and for 0.30% TS barrier (d)-(f) calculated using the numerical method and Eqs. (4.1)-(4.3).

QWire EAMs with LM Barrier QWire EAMs with 0.15% TS Barrier

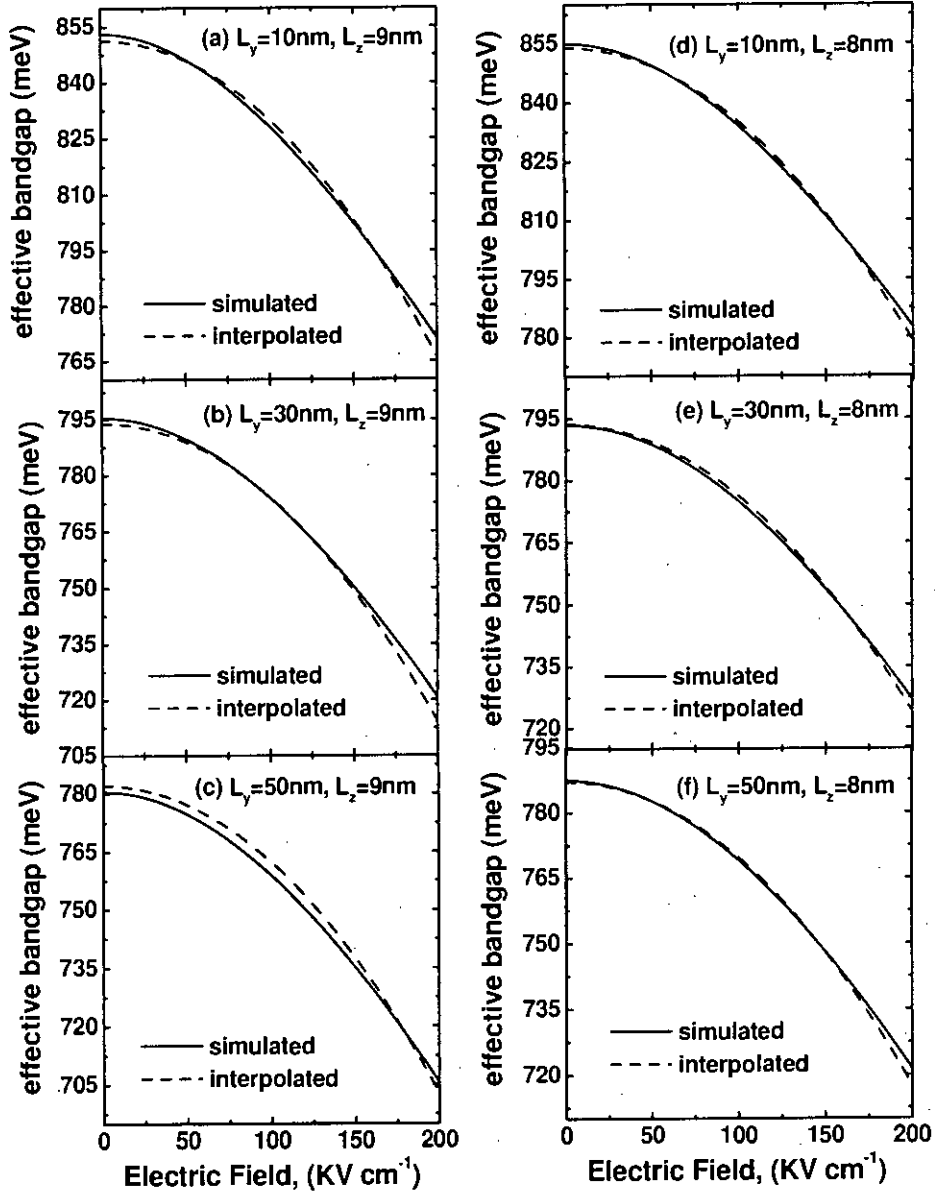


Figure 4.6: Electric field dependence of the effective bandgap in 10 nm, 30 nm, 50 nm for LM barrier with $L_z=9$ nm (a)-(c) and for 0.15% TS barrier with $L_z=8$ nm (d)-(f) calculated using the numerical method and Eqs. (4.1)-(4.3).

accurately. Therefore it is expected that these equations will be useful in designing QWire EAMs in a computationally efficient way.

4.3 Absorption Characteristics

Calculated transition matrix elements for the ground state transition M_{11} for transverse electric (TE) polarization with electric field along the wire axis ($TE_{||}$) in a 20 nm wide QWire for LM and two types of TS barriers as well as for different number of vertically stacked layers are presented in Fig. 4.7(a) and (b), respectively. Results indicate that with an increase in the barrier TS, transition strength is increased for the 1-1 transition. This is due to the fact that TS barriers suppress elastic strain relaxation. It is seen in Fig. 4.7(b) that multiple layer QWires show less transition strength compared to the single layer QWires due to more pronounced strain relaxation in multiple-layer QWires.

Fig. 4.8 shows the absorption spectra as a function of photon wavelength for 10 nm, 15 nm, 20 nm, 25 nm wide QWire EAMs considering 0.15% TS barriers. Both zero field and a typical $F_S = 125$ KV/cm are considered. With applied electric field, the absorption peaks move to longer wavelengths. With increasing electric field, as the overlap of electron and hole wavefunctions is reduced, absorption strength is reduced. It is also observed that the peaks of the absorption spectra are reduced with increasing wire width. Also, wider QWire EAMs show higher field sensitivity i.e., the amount of quantum confined Stark shift is higher in wider QWire EAMs than narrower QWire EAMs.

Fig. 4.9 shows the absorption spectra as a function of photon wavelength

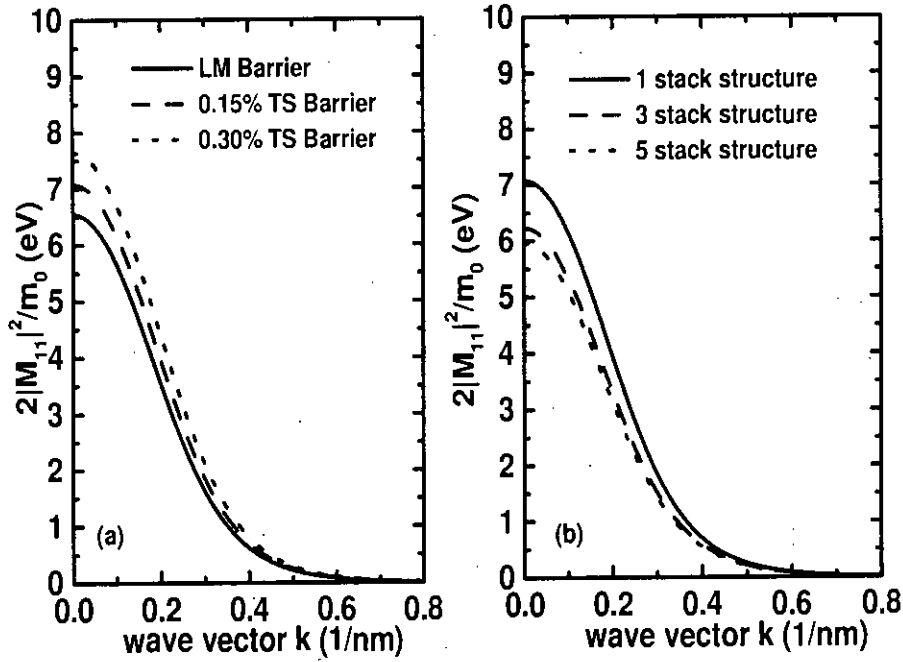


Figure 4.7: Transition matrix elements M_{11} as functions of wave vector k in a 20 nm wide QWire for three types of barriers (a) and for different number of QWire layers with 0.15% TS barriers (b). Only $TE_{||}$ polarization is considered.

for 20 nm (a), (b) and 30 nm (c), (d) wide QWire EAMs for two different types of barriers. LM and 0.15% TS barriers are considered. With the application of strain compensation in the barriers, the bandstructure shows a red shift consequently moving the absorption spectra to higher wavelength. The peak values of absorption increases with increasing strain compensation by the barriers. These results can be explained in terms of the barrier strain dependence of the transition matrix elements as presented in Fig. 4.7 (a).

Fig. 4.10 shows the absorption spectra per layer as a function of photon wavelength for 20 nm wide (a)-(c) and 30 nm wide (d)-(f) QWire EAMs

1S Structure with 0.15% TS Barrier

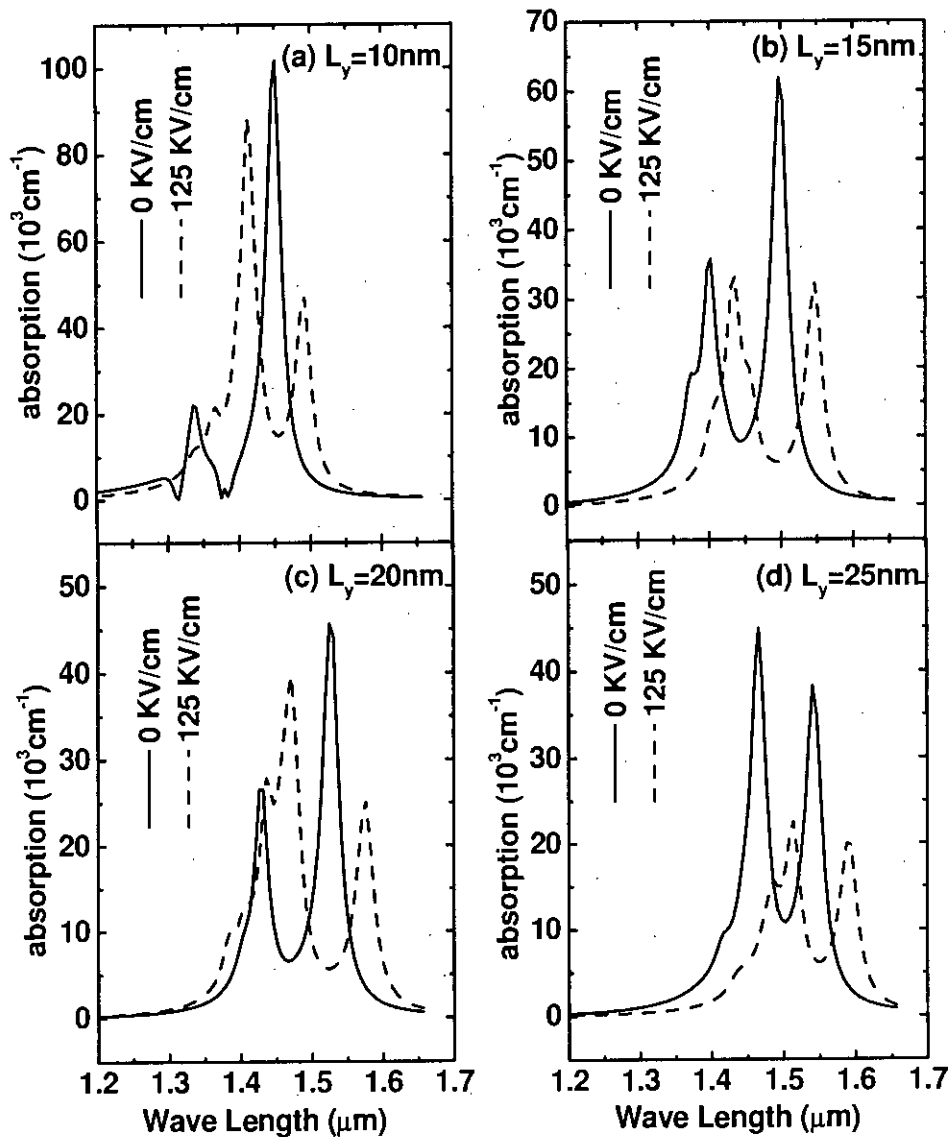


Figure 4.8: Absorption as a function of photon wavelength showing the effects of applied electric field in single layer QWire EAMs with 0.15% TS Barrier for different wire widths.

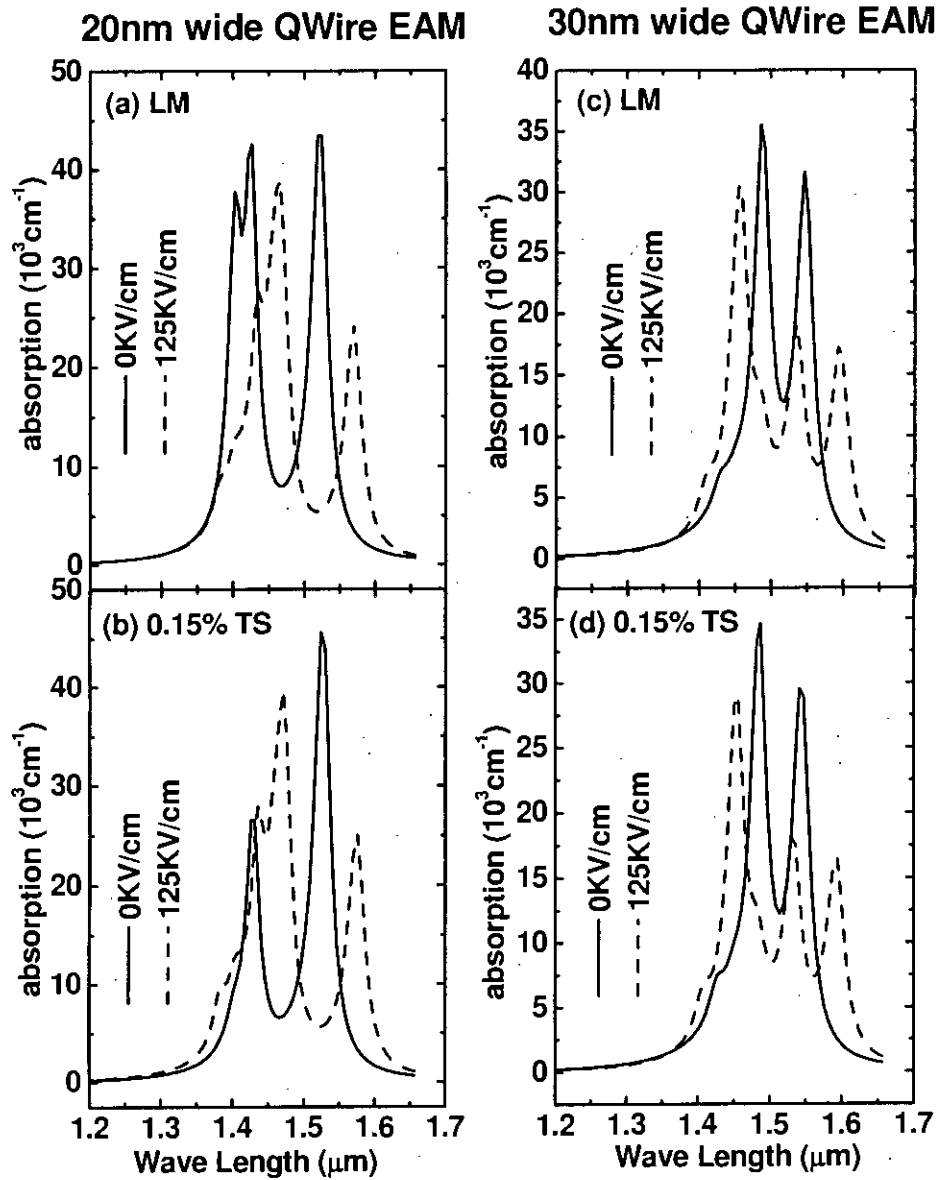


Figure 4.9: Absorption as a function of photon wavelength showing the effects of applied electric field in 20 nm wide QWire EAMs (a), (b) and 30 nm wide QWire EAMs (c), (d) for two different types of barriers. Single layer structure and both LM and 0.15% TS barriers are considered.

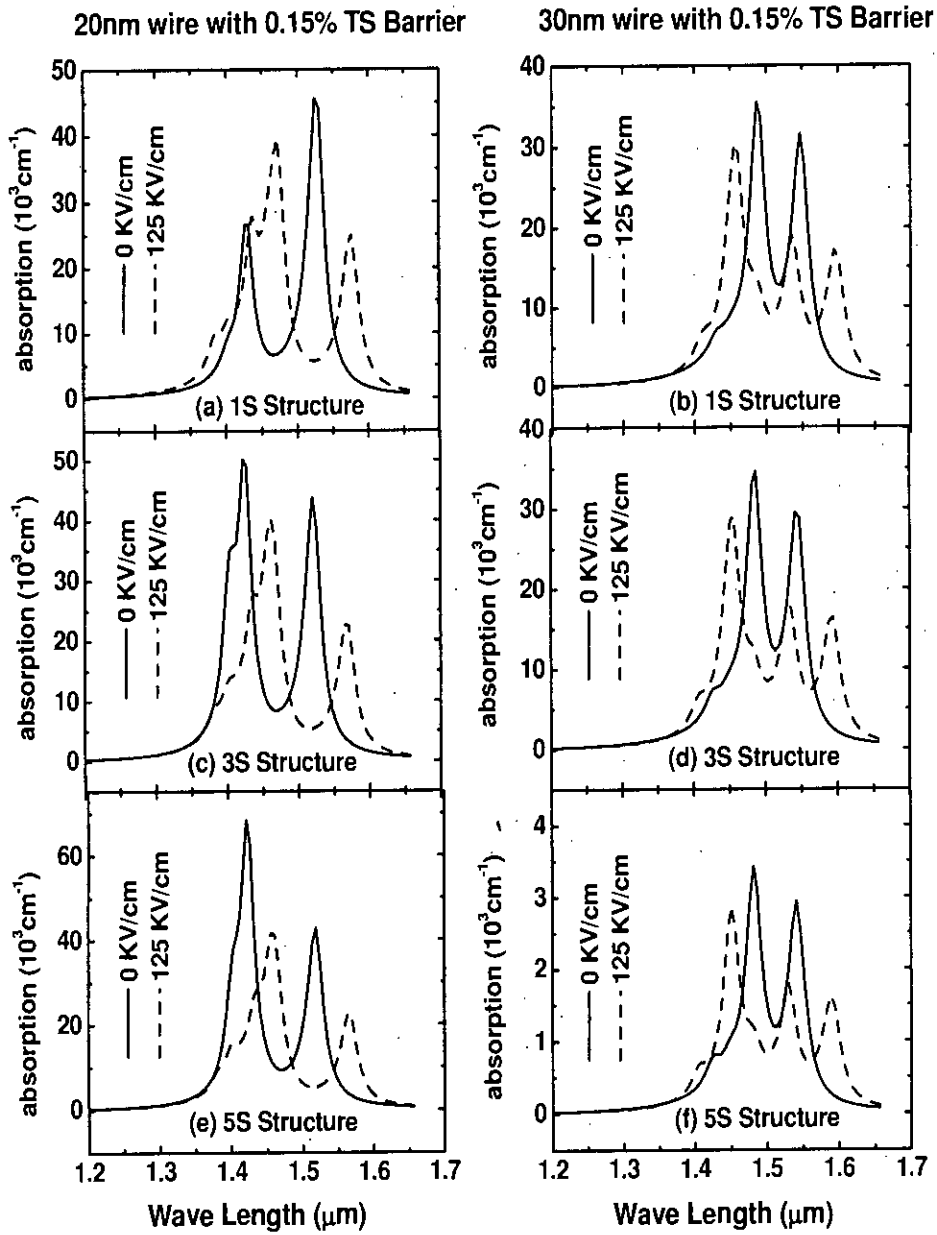


Figure 4.10: Absorption as a function of photon wavelength showing the effects of applied electric field in 20 nm wide QWire EAMs (a)-(c) and 30 nm wide QWire EAMs (d)-(f) with 0.15% TS barrier for different number of layers in the active regions.

10 nm wide QWire EAM with 0.15% TS barrier

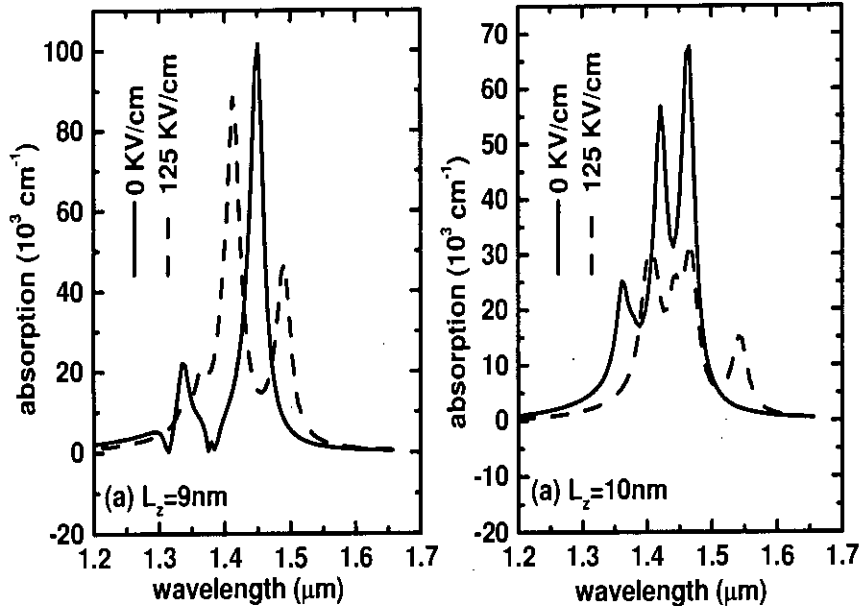


Figure 4.11: Absorption per layer as a function of photon wavelength showing the effects of applied electric field in a QWire EAMs with different wire height with 0.15% TS Barrier.

for different numbers of vertically stacked QWire layers in the active region. 0.15% TS barrier is considered. It is evident that with the introduction of multiple layers in the active region, ground state absorption per layer becomes weaker. This is due to the relatively weaker transition strengths of M_{11} in multiple layer structures as described in Fig. 4.7 (b).

Fig. 4.11 shows the absorption spectra as a function of photon wavelength for a 10 nm wide QWire EAM with different wire height. 0.15% TS barriers are considered. With the change of the wire height, shift in the absorption

Table 4.3: Extinction ratio of QWire and QWell EAMs with $L_z=7\text{nm}$ for $F_S=125\text{KV/cm}$. Length of the EAM section is $500\ \mu\text{m}$.

Barrier Strain	Device Structure	L_y (nm)	Operating Wavelength(μm)	Extinction Ratio	
				$L_P=100\text{nm}$	$L_P=200\text{nm}$
LM	QWire	10	1.455	18.9	9.45
	QWire	18	1.558	19.8	9.9
	QWire	30	1.594	21.4	10.7
	QWire	40	1.606	23.0	11.5
	QWire	50	1.613	25.7	12.8
	QWire	60	1.617	30.3	15.1
	QWire	80	1.622	26.0	13.0
	QWell			1.633	
0.15% TS	QWire	10	1.487	19.70	9.8
	QWire	15	1.545	20.7	10.4
	QWire	30	1.599	22.7	11.3
	QWire	40	1.611	24.2	12.1
	QWire	50	1.617	26.4	13.2
	QWire	60	1.621	30.6	15.3
	QWire	80	1.625	28.0	14.0
	QWell			1.640	

peak energies occur and consequently the desired $1.55\ \mu\text{m}$ wavelength may be achieved. However by increasing the wire height, the absorption peak is reduced. Through the proper choice of wire height, width, barrier strain compensation and operating electric field, it is shown that any desired operating wavelength around $1.55\ \mu\text{m}$ can be achieved.

Table. 4.3 presents the calculated extinction ratios for a number of QWire EAMs and comparison is made with QWell EAMs with similar structures. It is observed that significant increase in the extinction ratio can be achieved by adopting QWires in EAMs. In spite of having higher absorption peaks, narrower wires exhibit lower extinction ratios because of the reduced value of

the in-plane occupation factor, L_y/L_P . Extinction ratios of narrower wires can be increased by decreasing L_P . We also note that for $L_y \geq 80$ nm, extinction ratio has a decreasing trend with the increasing wire width.

Chapter 5

Conclusions

Performance of compressively strained (CS) GaInAsP/InP quantum wire (QWire) electro absorption modulators (EAMs) is theoretically investigated. A numerical method to analyze the device design guideline has been studied. An empirical relationship is proposed for the effective bandgap for quick and accurate estimation of the Stark shift.

5.1 Summary

The device structure consists of quaternary $\text{Ga}_x\text{In}_{(1-x)}\text{As}_y\text{P}_{(1-y)}$ grown on an (001) InP substrate. All the calculations are done for TE polarization of light which is dominant in CS structures. For QWires, the electric field of the radiation is assumed to be along the wire axis and the laser cavity is considered to be perpendicular to the wire axis.

In this work we have integrated the QWire EAMs with distributed feedback lasers integrated with distributed Bragg's reflectors on the same substrate. Recently the experimental realization of the device structure has been reported. A major advantage of this configuration is that due to the nature

of the integration the EAM is not required to be polarization insensitive. On the contrary, its polarization is naturally tuned to that of the QWire laser (TE in case of CS QWires). This leads to a considerable enhancement of the extinction ratio of the EAMs.

The electric field dependence of the effective bandgap of QWire EAMs (quantum confined Stark effect) is studied using an 8 band $k \cdot p$ theory including elastic strain relaxation effects. Elastic strain relaxation is calculated using an analytical approach. It is observed that the effect of the electric field is parabolic and an empirical relationship is proposed to quick estimation of the field induced shift in the effective bandgap, which is verified through numerical simulations. This relationship would be useful as a quick design guide for QWire EAMs.

Different quantities such as, the absorption coefficient, the extinction ratio and the operating wavelength are calculated as function of device parameters for performance analysis of the QWire EAMs to identify the improvement caused by the additional carrier confinement in QWires. It is observed that significant increase in the extinction ratio can be achieved by adopting QWires in EAMs. In spite of having higher absorption peaks, narrower wires exhibit lower extinction ratios because of the reduced value of the in-plane occupation factor, W/L_p . This situation may be improved by increasing the packing density of the QWires. We also note that for $W \geq 80\text{nm}$, extinction ratio has a decreasing trend with the increasing wire width.

Therefore, to optimize the device performance, it is necessary to investigate the device structures and also elastic strain relaxation and other important effects in detail.

5.2 Suggestions for Further Work

QWire structure in the active region of the EAMs have been investigated to identify the improvement caused by the additional carrier confinement than the QWell EAMs. Therefore, a future work can be done using QDot structure in the active region for further improvement of the device performance. The results of the empirical function are verified through numerical calculations. So, future work is necessary on experimental verification of the accuracy of the function in predicting the electric field dependence of the effective bandgap. In this work the simulation is done only on EAM section of the device assuming no propagation delay of the light output of the laser section to the EAM and the frequency response of the high capacitive laser diode has not been incorporated. Also the effects of DBR section and laser section on EAM operation have not been evaluated. Therefore, a future work can be done on simulating the total device structure as a whole incorporating the effects of laser section and DBR section on the EAMs.

Bibliography

- [1] L. A. Coldren and S. W. Corzine, "Diode lasers and photonic integrated circuits", NY: John Wiley & Sons, Chap. 8, 1995.
- [2] D. A. B. Miller, T. C. Damen, A. C. Gossard, W. Wiegmann, T. H. Wood, and C. A. Burus, "Band-edge electroabsorption in quantum well structures: The Quantum-confined Stark effect," *Phys. Rev. Lett.*, vol. 53, no. 22, pp. 2173-2176, Nov. 1984.
- [3] S. Z. Zhang, P. Abraham, and J. E. Bowers, "25 GHz polarization-insensitive electroabsorption modulators with traveling-wave electrodes," *IEEE Photon. Technol. Lett.*, vol. 11, pp. 191-193, Feb. 1999.
- [4] B. Pezeshki, S. M. Lord and J. S. Harris, "GaAs/AlAs quantum wells for electro-absorption modulators," *IEEE Trans. Electron Devices*, vol. 39, Issue. 11, pp. 2645-2646, Nov. 1992.
- [5] Y. J. Chiu, S. Z. Zhang, V. Kaman, J. Piprek, and J. E. Bowers, "High-speed traveling-wave electroabsorption modulators," *Proceedings of SPIE*, vol. 4490, pp. 1-10, 2001.
- [6] H. Yagi, T. Sano, K. Ohira, T. Maruyama, A. Haque, and S. Arai, "Room temperature-continuous wave operation of GaInAsP/InP

- multiple-quantum-wire lasers by dry etching and regrowth method," *Jpn. J. Appl. Phys.*, pt. 2, vol. 42, no. 7A, pp. 48-50, July 2003.
- [7] M. Asada, Y. Miyamoto, and Y. Suematsu, "Theoretical gain of quantum-well wire lasers," *Jpn. J. Appl. Phys.*, vol. 2, no. 2, pp. 95-97, Feb. 1985.
- [8] E. Yablonoitch, E. O. Kane, "Reduction of lasing threshold current density by lowering the valence band effective mass," *IEEE J. Light-wave Technol.*, vol. 4, pp. 504-506, May 1986.
- [9] A. R. Adams, "Band structure engineering for low-threshold high-efficiency semiconductor lasers," *IEEE Electron. Lett.*, vol. 22, pp. 249-250, 1986.
- [10] S. Ueno, Y. Miyake and M. Asada, "Advantage of strained quantum wire laser," *Jpn. J. Appl. Phys.*, vol. 31, pp. 286-287, 1992.
- [11] K. Ohira, T. Murayama, H. Yagi, S. Tamura and S. Arai, "Distributed reflector laser integrated with active and passive grating sections using lateral quantum confinement effect," *Jpn. J. Appl. Phys.*, vol. 42, no. 8, pp. 921-923, Aug. 2003.
- [12] K. Ohira, T. Murayama, H. Yagi, S. Tamura and S. Arai, "Low-threshold distributed reflector laser consisting of wide and narrow wirer like active regions," *IEEE Photon. Technol. Lett.*, vol. 17, no. 2, pp. 264-266, Feb. 2005.
- [13] E. E. Mendez, G. Bastard, L. L. Chang, L. Esaki, H. Morkoc and R. Fischer, "Effect of an electric field on the luminescence of GaAs

- quantum wells," *Phys. Rev. B*, vol. 26, no. 12, pp. 7101-7104, Dec. 1982.
- [14] M. Wiedenhaus, A. Ahland, D. Schulz and E. Voges, "Modelling and simulation of electroabsorption modulators," *IEEE Proc. Optoelectron.*, Vol 149, No 4, Aug. 2002.
- [15] S. A. Pappert, R. J. Orazi, T. T. Vu, S. C. Lin, A. R. Clawson and P. K. L. Yu, "Polarization dependence of a 1.52 μm InGaAs/InP multiple quantum well waveguide electroabsorption modulator," *IEEE Photon. Technol. Lett.*, vol. 2, no. 4, pp. 257-259, Apr. 1990.
- [16] K. Wakita, Y. Kawamura, Y. Yoshikumi, H. Asahi, S. Uehara, "Anisotropic electroabsorption and optical modulation in InGaAs/InAlAs multiple quantum well structures," *IEEE J. Quantum Electron.*, vol. QE-22, pp. 1831-1836, Sep. 1986.
- [17] T. Ido, H. Sano, D. J. Moss, S. Tanaka, A. Takai, "Strained InGaAs/InAlAs MQW electro-absorption modulators with large bandwidth and low driving voltage," *IEEE Photon. Technol. Lett.*, vol. 6, No. 10, pp. 1207-1209, Oct. 1994.
- [18] K. Wakita, I. Kotaka, K. Yoshino, S. Kondo and Y. Noguchi, "Polarization independent electroabsorption modulators using strain-compensated InGaAs-InAlAs MQW structures," *IEEE Photon. Technol. Lett.*, vol. 7, no. 12, pp. 1418-1420, Dec. 1995.
- [19] K. G. Ravikumar, T. Aizawa, and R. Yamauchi, "Polarization-independent field-induced absorption-coefficient variation spectrum in

- an InGaAs/InP tensile-strained quantum well," *IEEE Photon. Technol. Lett.*, vol. 5, no. 3, pp. 310-312, Mar. 1993.
- [20] K. Chang and J. B. Xia, "Quantum-confined Stark effects of exciton states in V-shaped GaAs/Al_xGa_{1-x}As quantum wires," *Phys. Rev. B*, vol. 58, no. 4, pp. 2031-2037, July 1998.
- [21] H. Weman, E. Martinet, M. A. Dupertuis, A. Rudra, K. Leifer and E. Kapon, "Two dimensional quantum-confined Stark effect in V-groove quantum wires: Excited state spectroscopy and theory," *Phys. Rev. Lett.* vol. 74, no. 16, pp. 2334-2336, Apr. 1999.
- [22] W. Huang, M. Xu and F. Jain, "1.55 μ m InGaAs-InP quantum wire optical modulators: Optimization Of wire width to maximize absorption and index of refraction changes due to excitonic transitions," *International J. Infrared and Millimeter Waves*, vol. 22, no. 7, pp. 1009-1018, Apr. 2001.
- [23] T. Arakawa, Y. Kato, F. Sogawa, and Y. Arakawa, "Photoluminescence studies of GaAs quantum wires with quantum confined Stark effect," *Appl. Phys. Lett.*, vol. 70, no. 5, pp. 646-648, Nov. 1996.
- [24] G. J. Vázquez, M. D. C. Mussot, H. N. Spector, "Tranverse Stark effect of electron in a semiconducting quantum wire," *Phys. Stat., sol.* (b) 240, no. 3, pp. 561-564, Oct. 2003.
- [25] J. M. Luttinger, and W. Kohn, "Motion of electrons and holes in perturbed periodic fields," *Phys. Rev.*, vol. 97, no. 4, pp. 869-876, Feb. 1955.

- [26] P. C. Sercel, and K. J. Vahalla, "Analytical formalism for determining quantum wire and quantum dot band structure in the multi-band envelope function approximation," *Phys. Rev.*, vol. 42, pp. 3690-3710, 1990.
- [27] G. Bastard and J. A. blum, "Electronic states in semiconductor heterostructure," *IEEE J. Quantum Electron.*, vol. QE-22, pp. 1625-1644, 1986.
- [28] E. O. Kane, "Energy band Theory," *In Handbook on Semiconductors*, vol. 1, W. Paul. Ed. Amsterdam, North Holland, pp. 193-217, 1982.
- [29] D. Gershoni, C. H. Henry and G. A. Baraff, "Calculating the optical properties of multidimensional heterostructures: Application to the modeling of quaternary quantum well lasers," *IEEE J. of Quantum Electron.*, vol. 29, no. 9, pp. 2433-2450, Sep. 1993.
- [30] L. M. Luttinger, "Quantum theory of cyclotron resonance in semiconductors: General theory," *Phys. Rev.*, vol. 102, pp. 1030-1041, 1956.
- [31] E. Yablonovitch, E. O. Kane, "Band structure engineering of semiconductor lasers for optical communications," *IEEE J. Lightwave Technol. Lett.*, vol. 6, no. 8, pp. 1292-1299, Aug 1988.
- [32] S. W. Corzine, R. Yan, and L. A. Coldren, "Optical gain in III-V bulk and quantum well semiconductors," in *Quantum Well Lasers*, P. Zory, Ed. New York: Academic Press, pp. 28-32, 1993.
- [33] R. E. Nahory, M. A. Pollack, and W. D. Johnston, Jr., "Bandgap versus composition and demonstration of Vegard's law for $\text{In}_{1-x}\text{Ga}_x\text{As}_y\text{P}_{1-y}$

- lattice matched to InP," *Appl. Phys. Lett.*, vol. 33, no. 7, pp. 659-661, Oct. 1978.
- [34] A. Haque, H. Yagi, T. Sano, T. Maruyama, and S. Arai, "Electronic band structures of GaInAsP/InP stacked multiple quantum wires with strain compensating barriers," *J. Appl. Phys.*, vol. 94, no. 3, pp. 2018-2023, Aug. 2003.
- [35] J. Downes and D. A. Faux, "Calculation of strain distributions in multiple-quantum-well strained-layered structures," *J. Appl. Phys.*, vol. 77, no. 6, pp. 2444-2447, Mar. 1995.
- [36] G. A. Baraff and D. Gershoni, "Eigenfunction-expansion method for solving the quantum wire problem: Formalism," *Phys. Rev.* vol. B43, pp. 4011-4022, 1991.
- [37] N. Nunoya, M. Nakamura, H. Yasumoto, S. Tamura, and S. Arai, "GaInAsP/InP multiple-layered quantum-wire lasers fabricated by CH₄/H₂ reactive-ion etching," *Jpn. J. Appl. Phys.*, pt. 1, vol. 39, no. 6A, pp. 3410- 3415, June 2000.
- [38] T. Ohtoshi, "Numerical analysis of α parameters and extinction ratios in InGaAsP/InP optical modulators," *IEEE J. Quantum Electron.*, vol. 9, no. 3, pp. 755-762, June 2003.

